# Interleukin-23 engineering improves CAR T cell function in solid tumors

Xingcong Ma[1,2,7], Peishun Shou[1], Christof Smith[1,3], Yuhui Chen[1], Hongwei Du[1], Chuang Sun[1], Nancy Porterfield Kren[1,4,5], Daniel Michaud[1,6], Sarah Ahn[1,3], Benjamin Vincent[1,3], Barbara Savoldo[1,3,6], Yuliya Pylayeva-Gupta[1,4,5], Shuqun Zhang[2], Gianpietro Dotti[1,3*] and Yang Xu[1,7*]

**Cytokines that stimulate T cell proliferation, such as interleukin (IL)-15, have been explored as a means of boosting the antitumor activity of chimeric antigen receptor (CAR) T cells. However, constitutive cytokine signaling in T cells and activation of bystander cells may cause toxicity. IL-23 is a two-subunit cytokine known to promote proliferation of memory T cells and T helper type 17 cells. We found that, upon T cell antigen receptor (TCR) stimulation, T cells upregulated the IL-23 receptor and the IL-23α p19 subunit, but not the p40 subunit. We engineered expression of the p40 subunit in T cells (p40-Td cells) and obtained selective proliferative activity in activated T cells via autocrine IL-23 signaling. In comparison to CAR T cells, p40-Td CAR T cells showed improved antitumor capacity in vitro, with increased granzyme B and decreased PD-1 expression. In two xenograft and two syngeneic solid tumor mouse models, p40-Td CAR T cells showed superior efficacy in comparison to CAR T cells and attenuated side effects in comparison to CAR T cells expressing IL-18 or IL-15.**

T cells can be rendered tumor specific via genetic engineering with a tumor-targeting TCR or a CAR[1]. TCR- and CAR-engineered T cells have promoted substantial objective clinical responses in synovial carcinoma[2] and B cell lymphoid malignancies[3], respectively. However, although CAR T cells expand in vivo in patients with B cell leukemia and can persist up to 24 months after infusion[4], in solid tumors, the suppressive tumor microenvironment (TME) usually hinders T cell expansion and persistence in multiple ways, such as by inducing checkpoint inhibition[5] and metabolic starvation[6] of T cells.

T cell proliferation requires optimal T cell activation, which integrates signals downstream of the TCR–CD3 complex, engagement of co-stimulatory molecules and cytokines[7]. CAR-based engineering provides stimulation through the TCR–CD3 complex and co-stimulatory molecules, whereas TCR-based engineering provides TCR engagement without adequate co-stimulation[7]. The cytokine component is a limiting factor for both TCR and CAR engineering strategies. The major pro-proliferative cytokine secreted by engineered T cells is IL-2, which may however support the activation and expansion of regulatory T ($T_{reg}$) cells[8], limiting antitumor effects. T cells have been engineered to express common γ-chain cytokines such as IL-15 in addition to the CAR, which is effective in supporting their proliferation and effector function while having only limited effects on $T_{reg}$ cells[9,10]. However, this type of cytokine engineering can lead to side effects, as the cytokines are constitutively produced and their receptors are expressed by most T cells and natural killer (NK) cells, requiring the inclusion of safety switches to contain potential toxic effects[11–13]. Thus, the development of inducible and selective engineering processes supporting T cell expansion and survival within the TME remains critical in adoptive T cell therapies in solid tumors for both TCR- and CAR-engineered T cells.

Most studies on the use of cytokines to support T cell immunotherapies have focused on STAT5-inducing cytokines, such as IL-2 and IL-15 (refs. [9,10,14,15]). In recent studies, STAT3 signaling enhanced CAR T cell effector function in preclinical models[16] and was associated with better clinical outcome in patients with chronic lymphocytic leukemia[17]. IL-23 is one of the STAT3-activating cytokines and consists of IL-23α p19 and IL-12β p40 subunits[18], both of which are expressed by activated macrophages and dendritic cells[19,20]. IL-23 is known to promote the proliferation of memory T cells and especially T helper type 17 ($T_H17$) cells expressing the IL-23 receptor (IL-23R)[19,21,22]. In particular, skewing CAR T cells toward a $T_H17$ profile by including the ICOS endodomain in the CAR construct has been shown to augment antitumor activity[23]. Here we found activation-induced expression of IL-23R and the IL-23α p19 subunit in T cells, which allowed us to couple the release and activity of IL-23 with T cell activation by supplementing T cells with the IL-12β p40 subunit. p40-expressing T cells (p40-Td cells) produce IL-23 upon T cell activation, which drives T cell proliferation and survival. Incorporating p40 in CAR- or TCR-engineered T cells enhanced their antitumor activity in xenograft and syngeneic mouse models. Furthermore, IL-23 produced by p40-Td cells functions predominantly through an autocrine mechanism, with limited effects on bystander cells. Our approach provides robust and selective proliferative signaling to adoptively transferred tumor-specific T cells within the TME.

## Results

**TCR–CD28 stimulation upregulates the expression of IL-23R in T cells.** We first evaluated whether IL-23R is expressed in T cells expanded ex vivo, following procedures used to generate CAR T cells for clinical use and that expand T cells phenotypically

[1]Lineberger Comprehensive Cancer Center, University of North Carolina at Chapel Hill, Chapel Hill, NC, USA. [2]Department of Oncology, Second Affiliated Hospital of Xi'an, Jiaotong University, Xi'an, China. [3]Department of Microbiology and Immunology, University of North Carolina at Chapel Hill, Chapel Hill, NC, USA. [4]Department of Genetics, University of North Carolina at Chapel Hill, Chapel Hill, NC, USA. [5]Department of Cell Biology and Physiology, University of North Carolina at Chapel Hill, Chapel Hill, NC, USA. [6]Department of Pediatrics, University of North Carolina at Chapel Hill, Chapel Hill, NC, USA. [7]These authors contributed equally: Xingcong Ma, Yang Xu. *e-mail: gdotti@med.unc.edu; dyyang@email.unc.edu

resembling memory T cells[24] (here collectively called ex-$T_M$ cells, expressing the CD45RO, CD27 and CD28 phenotypic markers). Although ex-$T_M$ cells expanded ex vivo at days 10–12 and rested from cytokines expressed low levels of IL-23R, stimulation of ex-$T_M$ cells with anti-CD3/CD28 antibodies upregulated IL-23R expression at both the mRNA and protein level (Fig. 1a,b). IL-23R expression in ex-$T_M$ cells was functional, as recombinant IL-23 supported the expansion of activated ex-$T_M$ cells, as previously observed in IL-23R$^+$ $T_H$17 cells[25], whereas ex-$T_M$ cells were irresponsive to IL-23 in the absence of TCR–CD28 stimulation (Fig. 1c). Furthermore, ex-$T_M$ cells responding to IL-23 were not polarized to $T_H$17 cells, as they showed a CD4$^+$/CD8$^+$ ratio similar to that of untreated T cells (Fig. 1d), retained a type I cytokine production profile (Fig. 1e) and showed T-bet and RORγT expression similar to that of untreated cells[26] (Fig. 1f). This lack of $T_H$17 polarization may be attributed to the restricted plasticity of ex-$T_M$ cells and/or the requirement for additional $T_H$17-skewing cytokines such as transforming growth factor (TGF)-β, IL-6 and IL-1β, as reported previously[27]. This selective activity of IL-23 without skewing toward a pathogenic $T_H$17 subset prompted us to explore whether the IL-23–IL-23R axis could be exploited to support the expansion of activated T cells within the TME.

**Functional engineering of the IL-23–IL-23R axis in T cells.** Unexpectedly, we observed that ex-$T_M$ cells upregulated the IL-23α p19 subunit upon TCR stimulation, but not the IL-12β p40 subunit (Fig. 1g). The observed inducible expression of both IL-23R and the IL-23α p19 subunit in ex-$T_M$ cells in response to TCR stimulation offers the unique opportunity to genetically engineer these cells with the IL-12β p40 subunit to produce and utilize IL-23 upon TCR stimulation. We supplemented ex-$T_M$ cells with the p40 subunit via gamma-retroviral transduction to generate p40-Td cells (Supplementary Fig. 1a). p40-Td cells, but not empty-vector-transduced T cells (Ctrl cells), secreted IL-23 upon TCR stimulation (Fig. 1h). Of note, p40-Td cells released limited amounts of IL-12 (~200 pg ml$^{-1}$ per $10^6$ cells), a cytokine that shares the p40 subunit with IL-23 (ref. [22]; Fig. 1h). In the absence of TCR–CD28 stimulation, p40-Td and Ctrl cells showed comparable phenotypic characteristics and expansion in culture (Supplementary Fig. 1b–e). In contrast, p40-Td cells showed superior expansion upon TCR–CD28 activation as compared to Ctrl cells (Fig. 1i). This effect could be attributed to both increased cell division (Supplementary Fig. 2a,b) and reduced apoptosis (Supplementary Fig. 2c). IL-23-mediated responses of p40-Td cells required the endogenous IL-23α subunit, as knockdown of *IL23A* mRNA by short hairpin RNA (shRNA) abolished both IL-23 production (Fig. 1j) and IL-23-mediated T cell expansion (Fig. 1k) in p40-Td cells. Even if p40-Td cells produced IL-12, the amount produced was low and did not induce IL-12 signaling in activated naive CD4$^+$ T cells (Supplementary Fig. 3a,b). Moreover, interferon (IFN)-γ production and *TBX21* gene expression were comparable in activated Ctrl and p40-Td cells (Supplementary Fig. 3c,d), confirming the absence of IL-12 signaling in p40-Td cells. Because of this unique activation-inducible nature of *IL23R* and *IL23A* expression, we further characterized the kinetics of their upregulation and IL-23 secretion. We found that both gene upregulation and IL-23 secretion were tightly linked to T cell activation. *IL23R* and *IL23A* expression and IL-23 secretion continued to increase with continued T cell stimulation up to day 5, but declined to baseline levels when T cells were removed from stimulation (Supplementary Fig. 4a–c). Furthermore, we also determined whether T cell activation through native TCR–major histocompatibility complex (MHC)/peptide engagement also induced *IL23R* and *IL23A* expression. We used T cells transduced to express a tyrosinase-specific TCR[28] and co-cultured them with T2 cells pulsed with tyrosinase peptide for 24 h. We found that both *IL23R* and *IL23A* were induced upon TCR engagement (Supplementary Fig. 4d), albeit at a lower level (for *IL23A*) than was seen following stimulation with anti-CD3/CD28 antibodies (Fig. 1g).

Previous studies showed elevated *IL23A* mRNA levels in tumor biopsies, suggesting a potential role for IL-23 in tumor progression,

**Fig. 1 | IL-23 supports the expansion of T cells in an activation-inducible manner. a**,**b**, IL-23R expression at the mRNA level measured by qRT–PCR (**a**) and at the protein level measured by western blot (**b**) in human T cells activated and expanded ex vivo (ex-$T_M$) at 0, 24 and 48 h after TCR activation. In **a**, data are represented as fold change in expression normalized to 18S RNA and to expression at time 0. Data are shown as individual values and the mean ± s.d. ($n = 6$ in **a** and $n = 5$ in **b**). **c**, Expansion of ex-$T_M$ cells with or without activation with anti-CD3/CD28 antibodies and with or without recombinant IL-23 (50 ng ml$^{-1}$). Cell numbers were determined by flow cytometry at day 7. Data are shown as individual values and the mean ± s.d. ($n = 4$). ***$P = 0.0002$, determined by repeated-measures two-way ANOVA with Sidak's post hoc test. Tx, treatment; NS, not significant. **d**, Distribution of CD4$^+$ and CD8$^+$ T cells among ex-$T_M$ cells activated with anti-CD3/CD28 antibodies in the presence or absence of 50 ng ml$^{-1}$ recombinant IL-23 at day 7. Data are shown as individual values and the mean ± s.d. ($n = 4$). **e**, Intracellular detection of IFN-γ and IL-17 in CD4$^+$ and CD8$^+$ T cells among ex-$T_M$ cells activated with anti-CD3/CD28 antibodies in the presence or absence of 50 ng ml$^{-1}$ recombinant IL-23 for 7 d. Data are shown as individual values and the mean ± s.d. ($n = 4$). **f**, Relative expression of the $T_H$17 and $T_H$1 transcription factors RORγT and T-bet, respectively, assessed by qRT-PCR in ex-$T_M$ cells activated with anti-CD3/CD28 antibodies in the presence or absence of 50 ng ml$^{-1}$ recombinant IL-23 for 7 d. Data are shown as individual values and the mean ± s.d. ($n = 4$). **g**, mRNA levels of the IL-23 p19 (*IL23A*) and p40 (*IL12B*) subunits in ex-$T_M$ cells activated with anti-CD3/CD28 antibodies at 0, 24 and 48 h, as determined by qRT–PCR. Data are expressed as fold change in expression, normalized to 18S RNA and to expression at time 0. Data are shown as individual values and the mean ± s.d. ($n = 4$). **h**, Detection of IL-23 secreted by Ctrl or p40-Td cells activated with anti-CD3/CD28 antibodies for 0, 24 and 48 h, as measured by ELISA. Data are shown as individual values and the mean ± s.d. ($n = 5$). ****$P < 0.0001$, determined by repeated-measures two-way ANOVA with Sidak's post hoc test. **i**, Numeric expansion of Ctrl and p40-Td cells activated with anti-CD3/CD28 antibodies. Data are shown as the mean ± s.d. ($n = 13$). ***$P = 0.0006$, ****$P < 0.0001$, determined by repeated-measures two-way ANOVA with Sidak's post hoc test. **j**, Detection of IL-23 secreted by activated Ctrl and p40-Td cells co-transduced with vector encoding either control shRNA (sh-Ctrl) or *IL23A*-targeted shRNA (sh-IL23A). Data are shown as individual values and the mean ± s.d. ($n = 3$). ***$P = 0.0002$, determined by repeated-measures two-way ANOVA with Sidak's post hoc test. **k**, Cell counts at day 5 for cells transduced with vector encoding sh-Ctrl or sh-IL23A activated with anti-CD3/CD28 antibodies. Data are shown as individual values and the mean ± s.d. ($n = 4$). **$P = 0.0069$ for Ctrl cells with sh-Ctrl versus p40-Td cells with sh-Ctrl, **$P = 0.0056$ for p40-Td cells with sh-Ctrl versus p40-Td cells with sh-IL23A, determined by repeated-measures two-way ANOVA with Sidak's post hoc test. **l**, Expression (transcripts per million) of *IL23A* (left) and *IL12B* (right) in tumor (red dots) and adjacent normal tissue (green dots) from different patients with cancer plotted using TCGA data. Highlighting of tumor types in red indicates higher expression in tumor versus normal tissue, whereas highlighting in green indicates lower expression in tumor versus normal tissue. **m**, Expression of *IL23A* and *IL12B* determined by qRT–PCR in breast cancer (BC), colorectal cancer (CRC) and pancreatic cancer (PC), together with paired adjacent normal tissue. Data are shown as copies of RNA per 50 ng of RNA ($n = 6$). The dotted line indicates the detection limit of the qRT–PCR assay used ($C_T > 35$). **$P = 0.0019$, determined by one-way ANOVA with Sidak's post hoc test. **n**, Detection of IL-23 by ELISA in the supernatant of single-cell suspensions of paired tumor and adjacent normal tissues. Data are shown as pg of IL-23 per 100 μg of supernatant protein, with individual values and the mean ($n = 6$).

especially in colorectal carcinoma (CRC)[29,30]. However, because IL-23 is a heterodimeric protein, both the IL-23α and IL-12β subunits must be present in the same cell to produce and release IL-23. Analysis of RNA-seq data from The Cancer Genome Atlas (TCGA) showed that, whereas the *IL23A* transcript was upregulated in many tumor specimens, the *IL12B* transcript was barely detectable in both tumor and normal tissue specimens (Fig. 1l), predicting an absence of IL-23 within the TME. We also measured expression

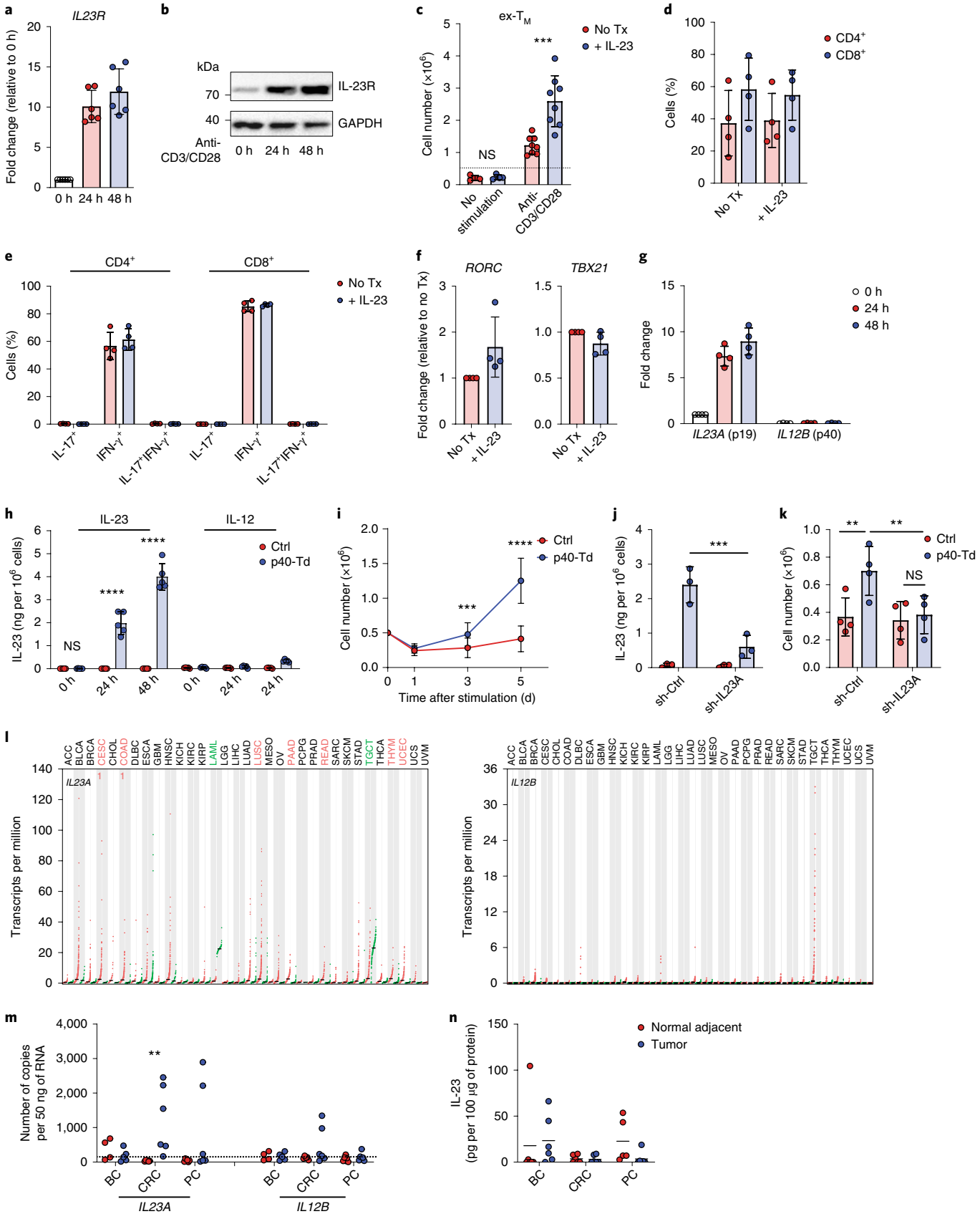

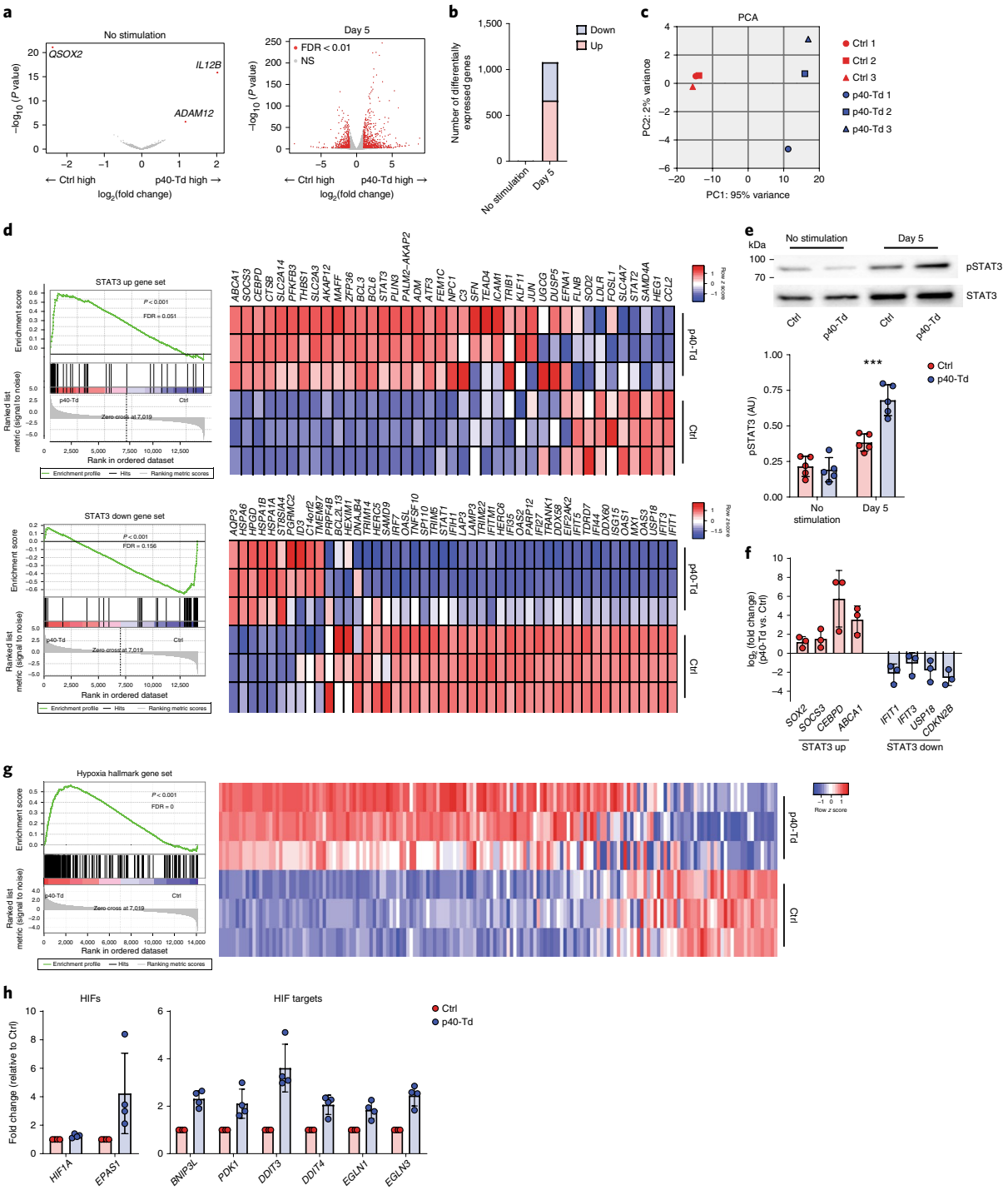


**Fig. 2 | TCR activation induces a STAT3 and hypoxia gene signature in p40-Td cells. a**, Volcano plots of gene expression before activation (left) and 5 d after activation (right) with anti-CD3/CD28 antibodies of Ctrl and p40-Td cells ($n = 3$). Volcano plots were constructed using $\log_2$(fold change) and $-\log_{10}$(FDR) values for all genes. Red dots represent genes with more than a twofold change (up or down) in expression and FDR < 0.01. **b**, Numbers of differentially expressed genes before and after stimulation of Ctrl and p40-Td cells. **c**, Principal-component analysis (PCA) of activated Ctrl and p40-Td cells ($n = 3$). **d**, GSEA for the expression profiles of activated Ctrl cells as compared to activated p40-Td cells using 'STAT3 upregulated' (up) and 'STAT3 downregulated' (down) gene sets and expression heat maps of genes in these gene sets ($n = 3$). Nominal $P$ values and FDR $q$ values were calculated using GSEA software (Broad Institute). **e**, Top: representative western blots showing Ser727 and Tyr705 phosphorylation of STAT3 in Ctrl and p40-Td cells before and 5 d after stimulation with anti-CD3/CD28 antibodies. Bottom: densitometry of phosphorylated STAT3, with data shown as individual values and the mean ± s.d. ($n = 5$). ***$P = 0.0001$, determined by repeated-measures two-way ANOVA with Sidak's post hoc test. **f**, qRT–PCR quantification of upregulated (red) and downregulated (blue) genes related to the STAT3 pathway. Data were first normalized to 18S RNA and are shown as the mean ± s.d. of the $\log_2$(fold change) in gene expression for activated Ctrl cells versus p40-Td cells ($n = 4$). **g**, GSEA for the expression profiles of activated Ctrl and p40-Td cells using the 'hallmark of hypoxia' gene set (left) and an expression heat map of genes in the gene set (right) ($n = 3$). The nominal $P$ value and FDR $q$ value were calculated using GSEA software (Broad Institute). **h**, qRT–PCR quantification of hypoxia-pathway-related genes in activated Ctrl and p40-Td cells. Data were first normalized to 18S RNA and then to the expression level in Ctrl cells. Data are shown as individual values and the mean ± s.d. ($n = 4$).

of the IL-23 subunits at the mRNA and protein level by qPCR and ELISA, respectively, in 18 tumor specimens (CRC, pancreatic ductal adenocarcinoma (PDAC) and breast cancer). Whereas the *IL23A* gene was upregulated in CRC tumor specimens, *IL12B* was not expressed (Fig. 1m) and IL-23 was absent from most of the supernatants obtained from CRC specimens (Fig. 1n). Therefore, IL-23 p40 engineering of T cells may support T cell expansion in a TCR-activation-dependent manner within the TME, which is deprived of IL-23.

**Transcriptome analysis of activated p40-Td cells reveals a signature enriched for STAT3 and hypoxia genes.** We performed RNA-seq analysis to define the molecular pathways involved in p40-Td cells. Ctrl cells and p40-Td cells had similar gene expression profiles in the absence of TCR stimulation (Fig. 2a). In contrast, after TCR activation, p40-Td cells showed a different molecular signature as compared to Ctrl cells (Fig. 2a–c), indicating the requirement for TCR stimulation to fully exploit the effects of the engineered IL-23–IL-23R axis in ex-$T_M$ cells. Specifically, gene set enrichment analysis (GSEA)[31] showed a significant enrichment of STAT3-upregulated genes in activated p40-Td cells and STAT3-downregulated genes in Ctrl cells (Fig. 2d), suggesting elevated STAT3 activity in p40-Td cells. The molecular signature was validated by detecting increased STAT3 phosphorylation in activated p40-Td cells (Fig. 2e) and differential expression of STAT3-regulated genes (*SOX2*, *SOCS3*, *CEBPD*, *ABCA1*, *IFIT1*, *IFIT3*, *USP18* and *CDKN2B*) (Fig. 2f). Furthermore, we observed an enrichment for genes within the hypoxia hallmark gene set in TCR-stimulated p40-Td cells as compared to Ctrl cells (Fig. 2g) and mRNA upregulation of hypoxia-inducible factors (HIFs) and other HIF target genes (Fig. 2h). Overall, these data highlight activation of the STAT3 pathway upon TCR activation in p40-Td cells, indicating a dominant role for IL-23 signaling in these cells.

**p40 expression enhances the antitumor activity of CAR T cells in xenograft models of solid tumors.** We assessed whether IL-23 p40 expression in CAR T cells improves their antitumor activity. We expressed p40 in CAR T cells (CAR.p40-Td cells) targeting the GD2 antigen expressed in neuroblastoma (Supplementary Fig. 5a,b). CAR.p40-Td cells showed robust expansion (Supplementary Fig. 5c) and reduced apoptosis (Supplementary Fig. 5d) when stimulated in vitro with an anti-idiotype antibody that cross-links the CAR[32], as compared to control CAR T cells (CAR.Ctrl cells). IL-23 was only detected in activated CAR.p40-Td cells, whereas IL-2 secretion remained unchanged (Supplementary Fig. 5e). The antitumor effects of CAR T cells in vitro were assessed by repetitive tumor co-culture assays in which human neuroblastoma cell lines (LAN-1 and CHLA-255) were used at a high tumor to T cell ratio (Supplementary Fig. 6a). In this stress culture condition test, CAR.Ctrl cells failed to control tumor growth after the first or second round of co-culture, whereas CAR.p40-Td cells remained effective (Fig. 3a,b). In parallel, the number of CAR.Ctrl cells was gradually reduced after each round of co-culture, whereas CAR.p40-Td cells persisted and retained CAR expression (Fig. 3c,d and Supplementary Fig. 6b). In addition to enhanced proliferation, CAR.p40-Td cells showed superior effector function at the individual cell level. Specifically, CAR.p40-Td cells expressed higher levels (as evaluated by percentage and mean fluorescence intensity (MFI)) of the lytic enzyme granzyme B (Fig. 3e) and reduced expression of the exhaustion markers PD-1 and CD101 (ref. [33]; Fig. 3f), as compared to CAR.Ctrl cells. In addition, after repeated stimulation, CAR.Ctrl cells exhibited a progressive reduction in the percentage of T cells producing IFN-γ and TNF-α, an indicator of functional exhaustion[34], whereas CAR.p40-Td cells continued to produce IFN-γ and TNF-α (Fig. 3g). In a metastatic neuroblastoma model in NOD-SCID-IL-2R$^{null}$ (NSG) mice, treated with suboptimal doses ($2\times10^6$ cells) of CAR T cells, CAR.p40-Td cells promoted enhanced tumor control and improved survival as compared to CAR.Ctrl cells (Fig. 3h–k). In line with this, CAR.p40-Td cells showed superior initial expansion (day 10) in vivo in peripheral blood, spleen and liver (Fig. 3l) and prolonged persistence in the same organs at the time that mice were killed (Fig. 3m). When a higher dose ($4\times10^6$ cells) of CAR T cells was used in tumor-bearing mice, both CAR.Ctrl and CAR.p40-Td cells promoted tumor regression (Fig. 3n–p), but only mice receiving CAR.p40-Td cells were protected from tumor re-challenge 4 weeks after T cell treatment (Fig. 3n–p). Notably, the enhanced antitumor activity provided by p40 overexpression was not restricted to CAR T cells cultured ex vivo with IL-7 and IL-15 (Supplementary Fig. 6c)

**Fig. 3 | p40 expression enhances the antitumor activity of CAR T cells in a neuroblastoma model. a**,**b**, Counts of LAN-1 (**a**) and CHLA-255 (**b**) neuroblastoma tumor cells after each round of repetitive co-culture (rounds 1–3, R1–R3) with control T cells (Ctrl), GD2-specific CAR T cells (CAR.Ctrl) or GD2-specific CAR T cells coexpressing p40 (CAR.p40-Td). Data are shown as individual values and the mean ± s.d. ($n=8$). ****$P<0.0001$, determined by repeated-measures two-way ANOVA with Sidak's post hoc test. **c**,**d**, T cell counts after each round of repetitive co-culture illustrated in **a** and **b**. Data are shown as individual values and the mean ± s.d. ($n=8$). *$P=0.03$ for LAN-1 round 2, **$P=0.0049$ for LAN-1 round 3, ***$P=0.0003$ for CHLA-255 round 2, **$P=0.0091$ for CHLA-255 round 3, determined by repeated-measures two-way ANOVA with Sidak's post hoc test. **e**, Intracellular staining for granzyme B of CAR.Ctrl and CAR.p40-Td cells at the end of round 1. Data are shown as individual values and the mean ± s.d. ($n=3$). **$P=0.0052$, determined by two-sided paired *t*-test. **f**, Expression of PD-1 and CD101 in CAR.Ctrl and CAR.p40-Td cells after rounds 1 and 2 of repetitive co-culture with LAN-1 tumor cells. Data are shown as individual values and the mean ± s.d. ($n=3$). **$P=0.0014$ for PD-1 round 2, *$P=0.0365$ for CD101 round 2, determined by repeated-measures two-way ANOVA with Sidak's post hoc test. AU, arbitrary units. **g**, Intracellular staining for IFN-γ and TNF-α of CAR.Ctrl and CAR.p40-Td cells at the end of rounds 1 and 2 of co-culture with LAN-1 tumor cells. Data are shown as individual values and the mean ± s.d. ($n=3$). **$P=0.002$ for IFN-γ$^+$ cells round 1, *$P=0.0409$ for IFN-γ$^+$TNF-α$^+$ cells round 1, ****$P<0.0001$ for IFN-γ$^+$ cells round 2, **$P=0.009$ for IFN-γ$^+$TNF-α$^+$ cells round 2, determined by repeated-measures two-way ANOVA with Sidak's post hoc test. **h**, Schematic of the metastatic neuroblastoma xenograft model; i.v., intravenous. **i**, Representative tumor bioluminescence from two independent experiments. IVIS, imaging (using IVIS Lumina II in vivo imaging system). **j**, Kinetics of tumor bioluminescence from two independent experiments ($n=8$ mice for the Ctrl group, $n=9$ mice per group for the CAR.Ctrl and CAR.p40-Td groups). Thick lines delineate mean fold change over time, while thin lines show data for each individual mouse. **k**, Kaplan–Meier survival curves summarizing two independent experiments ($n=8$ mice per group). ****$P<0.0001$. **l**, Frequency of human CD3$^+$CD45$^+$ cells in blood, spleen and liver collected 10 d after T cell infusion. Data are shown as individual values and the mean ($n=5$ mice per group) and are representative of two experiments. ***$P=0.0006$ for blood, ****$P<0.0001$ for liver, ***$P=0.0007$ for spleen, determined by one-way ANOVA with Sidak's post hoc test. **m**, Frequency of human CD3$^+$CD45$^+$ cells in blood, spleen and liver collected at the time that mice were killed (median collection time: 18, 22 and 52 days post T cell infusion for the Ctrl, CAR.Ctrl and CAR.p40-Td groups, respectively). Data are shown as individual values and the mean ($n=5$ mice per group) and are representative of two experiments. *$P=0.0132$ for blood, **$P<0.0067$ for liver, **$P=0.0071$ for spleen, determined by one-way ANOVA with Sidak's post hoc test. **n**, Schematic of the metastatic neuroblastoma xenograft model and tumor re-challenge. **o**, Representative tumor bioluminescence from two independent experiments. **p**, Kinetics of tumor bioluminescence from two independent experiments ($n=6$ mice for the Ctrl group, $n=7$ mice per group for the CAR.Ctrl and CAR.p40-Td groups). Thick lines delineate mean fold change over time, while thin lines show data for each individual mouse.

nor to CAR T cells encoding the CD28 co-stimulatory endodomain (Supplementary Fig. 7). Moreover, the enhanced antitumor activity of CAR.p40-Td cells was confirmed in a PDAC model using CAR T cells targeting the B7-H3 antigen (Supplementary Fig. 8)[35]. CAR.p40-Td cells showed superior antitumor effects and better persistence in stressed co-culture conditions against the human PDAC cell line BXPC-3 in comparison to CAR.Ctrl cells (Fig. 4a,b). Furthermore, in an orthotopic PDAC model using the BXPC-3 cell

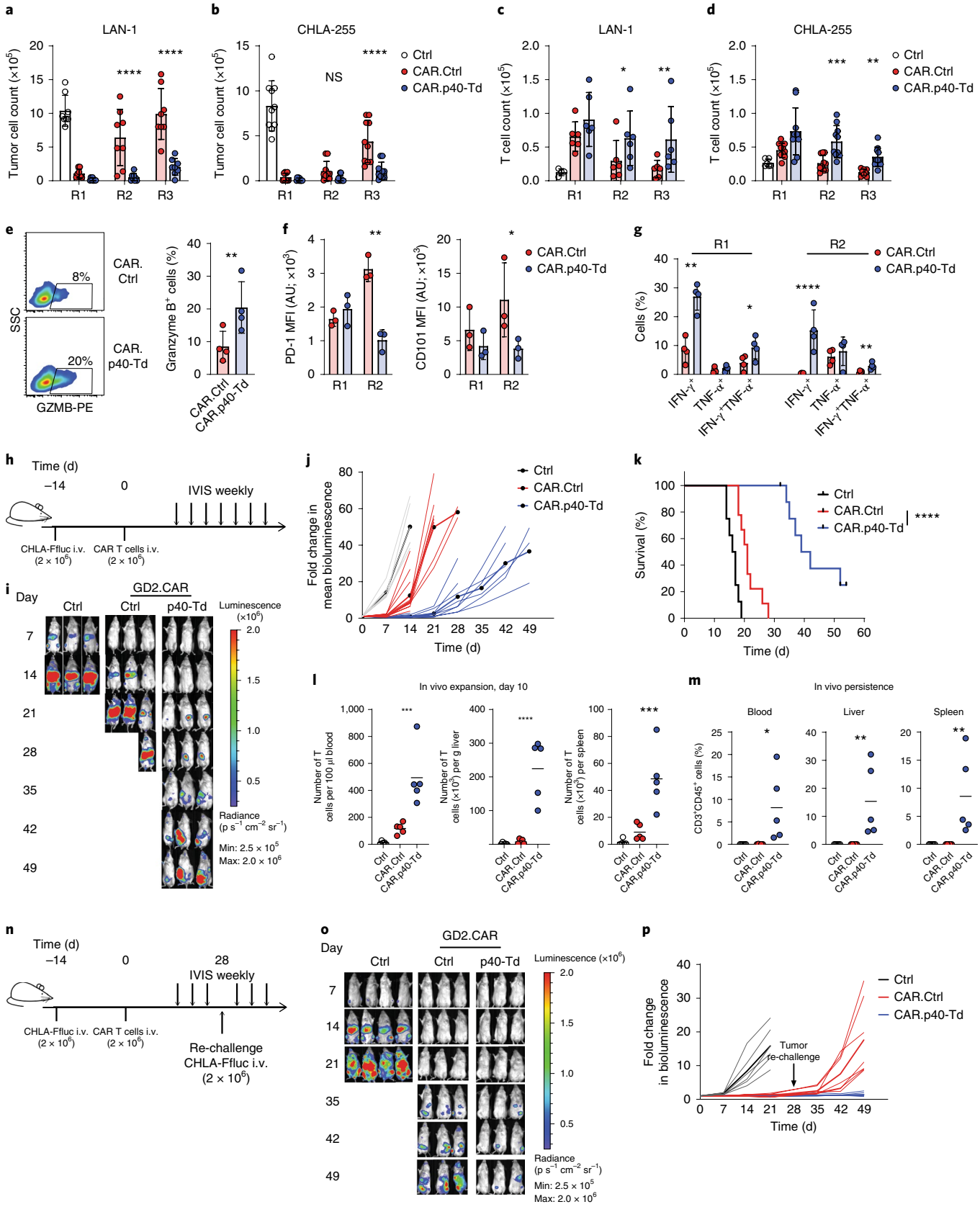

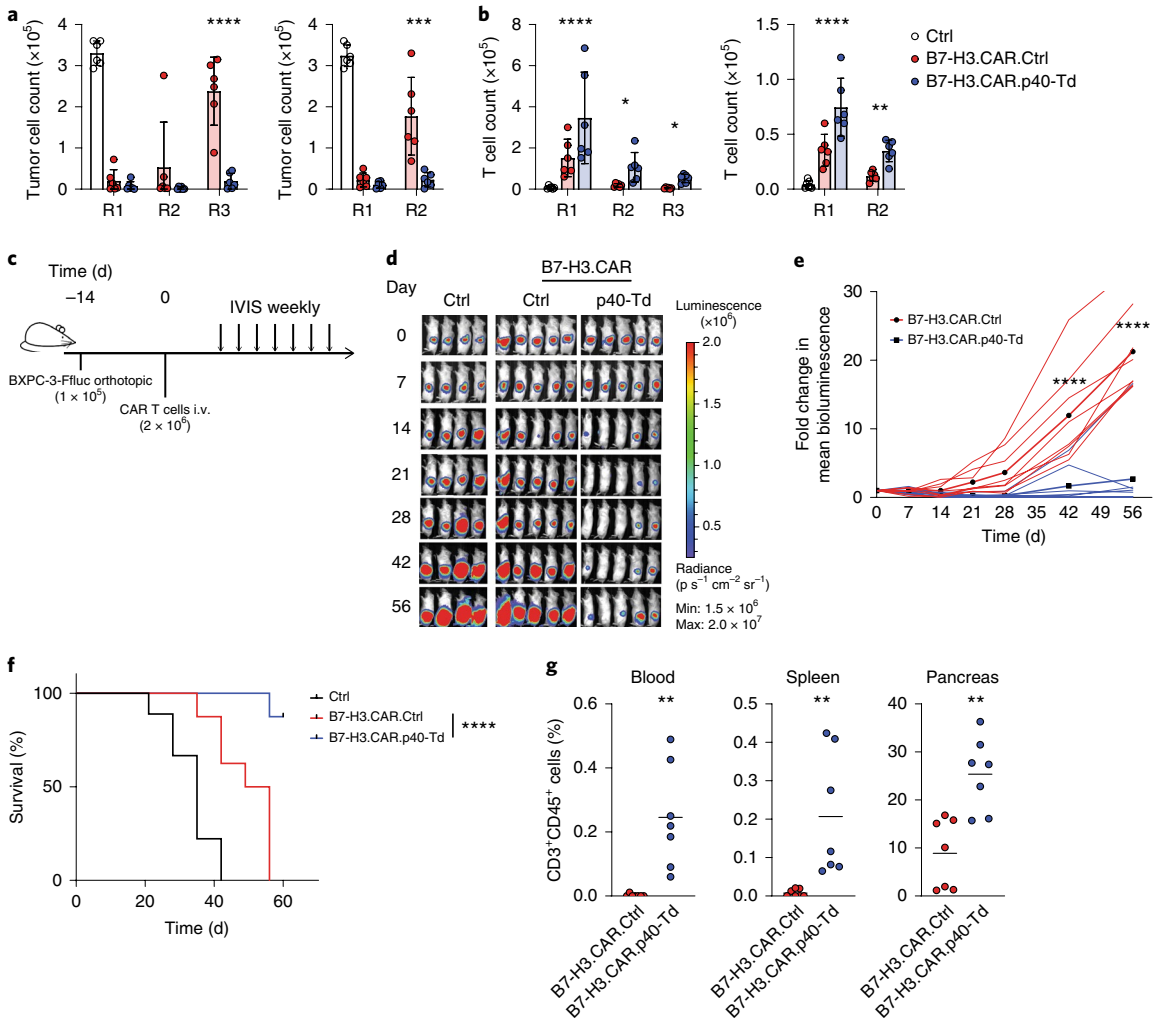


**Fig. 4 | p40 expression enhances the antitumor activity of CAR T cells in a pancreatic cancer model. a**, Counts of pancreatic cancer (BXPC-3) cells after each round of repetitive co-culture with Ctrl T cells, B7-H3-specific CAR T cells (CAR.Ctrl) or B7-H3-specific CAR T cells coexpressing p40 (CAR.p40-Td) at a T cell to tumor cell ratio of 1:2 (left) or 1:5 (right). Data are shown as individual values and the mean ± s.d. ($n = 6$). ***$P = 0.0003$, ****$P < 0.0001$, determined by repeated-measures two-way ANOVA with Sidak's post hoc test. **b**, T cell counts after each round of repetitive co-culture in **a**. Data are shown as individual values and the mean ± s.d. ($n = 6$). *$P = 0.0195$ for round 2 with a 1:2 ratio, *$P = 0.021$ for round 3 with a 1:2 ratio, **$P = 0.0024$ for round 2 with a 1:5 ratio, ****$P < 0.0001$, determined by repeated-measures two-way ANOVA with Sidak's post hoc test. **c**, Schematic of the orthotopic pancreatic cancer model. **d**, Representative tumor bioluminescence from two independent experiments ($n = 8$ mice per group). **e**, Kinetics of tumor bioluminescence from two independent experiments ($n = 8$ mice per group). Thick lines delineate mean fold change over time, while thin lines show data for each individual mouse. ****$P < 0.0001$. **f**, Kaplan–Meier survival analysis for two independent experiments ($n = 8$ mice per group). ****$P < 0.0001$. **g**, Frequency of human CD3$^+$CD45$^+$ cells in blood, spleen and pancreas collected from mice at day 60 after T cell infusion. Data are shown as individual values and the mean ($n = 7$ mice per group from two independent experiments). **$P = 0.0017$ for blood, **$P = 0.00065$ for spleen, **$P = 0.0014$ for pancreas, determined by two-sided unpaired Student's *t*-test.

line that constitutively expresses high levels of PD-L1 and is more resistant to CAR T cell effects[35], CAR.p40-Td cells showed superior antitumor effects and better persistence when compared to CAR. Ctrl cells (Fig. 4c–g and Supplementary Fig. 8b,c). Therefore, p40 engineering of CAR T cells promotes antitumor activity, sustaining T cell persistence and expansion.

**Incorporation of p40 in mouse T cells promotes local effects of IL-23 in syngeneic tumor models of melanoma and pancreatic cancer.** To evaluate the effects of IL-23 in immune-replete mice, we implemented syngeneic tumor models. We first confirmed that *Il23r* and *Il23a*, but not *Il12b*, were inducible in ex vivo-activated mouse T cells that resembled human ex-$T_M$ cells generated for adoptive T cell transfer (Fig. 5a,b). Recapitulating the observations in human ex-$T_M$ cells, gene transfer of the mouse *Il12b* gene into mouse T cells resulted in activation-inducible IL-23 secretion (Fig. 5c) and enhanced T cell expansion (Fig. 5d) in vitro upon TCR stimulation. We tested the antitumor effects of mouse T cells expressing the mouse p40 subunit using the B16-OVA melanoma mouse model and adoptive transfer of ex vivo-expanded OT-1 T cells (Fig. 5e). When B16-OVA-bearing mice were treated with suboptimal doses ($1 \times 10^6$ cells per mouse) of OT-1 T cells, OT-1 T cells engineered to express p40 (OT-1-mp40-Td cells) showed superior tumor control as compared to OT-1 T cells transduced with empty vector (OT-1-EV cells) (Fig. 5f, left). Treatment with a higher dose ($2 \times 10^6$ cells per mouse) of OT-1-mp40-Td cells resulted in sustained tumor control up to 30 d after tumor inoculation (Fig. 5f, right). Notably, IL-23 was detected only in supernatant obtained from the tumor and not in the serum of mice treated with OT-1-mp40-Td cells (Fig. 5g). Correspondingly, in mice infused with OT-1-mp40-Td

cells, we observed a higher percentage of CD8$^+$ OT-1 T cells within the tumor, but not in the blood, spleen or tumor draining lymph node (dLN), where the frequency of OT-1 T cells was similar to that in mice receiving control OT-1-EV T cells (Fig. 5h). Furthermore, no alteration in the composition of CD4$^+$ and CD8$^+$ T cells, B cells, NK cells or myeloid cells was observed in the blood, spleen, tumor or dLN (Fig. 5i). To further validate our approach using CAR T cells, we used our previously established syngeneic PDAC model and B7-H3-specific CAR T cells[35] (Fig. 5j). Specifically, the KPC-4662 PDAC cell line expressing mouse B7-H3 was orthotopically engrafted into C57BL/6 mice. As previously reported, the engrafted tumors hosted a comprehensive immune microenvironment that included B cells, $T_{reg}$ cells, macrophages, Gr1$^+$ myeloid-derived suppressor cells and tumor-associated fibroblasts (Supplementary Fig. 9)[36–38]. Upon engraftment, mice were treated with mouse T cells expressing the B7-H3-specific CAR (Supplementary Fig. 10) and transduced with either empty vector (B7-H3.CAR.EV) or vector encoding the mouse p40 subunit (B7-H3.CAR.mp40-Td). Mice treated with B7-H3.CAR.mp40-Td cells showed significantly better tumor control than mice treated with B7-H3.CAR.EV cells (Fig. 5k). Collectively, we demonstrated that p40 engineering in mouse T cells expressing a tumor-specific TCR or CAR exerts a local effect that enhances antitumor activity without disturbance of global immune composition.

**CAR T cells equipped with p40 show superior antitumor efficacy and safety in comparison to CAR T cells engineered with IL-18 or IL-15.** Incorporation of cytokines such as IL-18 (refs. [39–41]) and IL-15 (ref. [42]) into CAR constructs improves the antitumor activity of CAR T cells. Therefore, we performed a side-by-side comparison between CAR.p40-Td cells and CAR T cells engineered with either IL-18 (CAR.IL18-Td) or IL-15 (CAR.IL15-Td). CAR.p40-Td cells showed the most prominent cell expansion following CAR stimulation in vitro (Supplementary Fig. 11a), while CAR.IL15-Td cells showed some level of activation-independent cell proliferation, as previously described[42] (Supplementary Fig. 11b). CAR.p40-Td cells also showed more consistent and prolonged tumor control in repetitive co-culture assays (Supplementary Fig. 11c). In the metastatic neuroblastoma model in immunodeficient mice, using low CAR T cell doses ($2\times10^6$ cells), CAR.p40-Td cells showed better antitumor control without any apparent side effects, as compared to mice treated with CAR.IL18-Td or CAR.IL15-Td cells, which, despite showing antitumor activity, caused weight loss (Supplementary Figs. 12 and 13). We further corroborated the superior antitumor activity of p40 versus IL-18 and IL-15 in the B16-OVA–OT-1 immunocompetent mouse model (Supplementary Fig. 14). Collectively, tumor-specific T cells equipped with p40 outperformed tumor-specific T cells coexpressing either IL-18 or IL-15 with respect to both antitumor activity and safety.

**Engineered IL-23 functions predominantly through an autocrine mode of action.** To better characterize the mode of action of IL-23 in p40-expressing T cells, we mixed p40-Td cells, which were tagged with a truncated form of NGFR (NGFR$^+$)[43], in vitro with control T cells tagged with a truncated form of CD19 (ΔCD19-Td)[44] at a 1:1 ratio and stimulated the mixed cells with anti-CD3/CD28 antibodies (Fig. 6a). Despite the two cell types having the same culture medium containing IL-23, expressing comparable levels of IL-23R (Fig. 6b) and being equally responsive to exogenously supplemented IL-23 (Supplementary Fig. 15a), p40-Td cells expanded more than ΔCD19-Td cells (Fig. 6c,d). Similarly, in multiple-round co-culture assays with mixed CAR.p40-Td cells and control CAR.ΔCD19-Td cells, CAR.p40-Td cells preferentially expanded in response to tumor cells as compared to control CAR T cells (Fig. 6e,f). To further study the self-beneficial effects of IL-23 in p40-Td cells, we evaluated whether IL-23 produced by p40-Td cells preferentially bound to the IL-23R expressed by p40-Td cells rather than the IL-23R expressed by bystander cells. We generated a p40–GFP fusion protein that allowed us to track the location of IL-23 (p19 and p40–GFP heterodimer) produced by T cells (Fig. 6g). We co-cultured T cells transduced to express p40–GFP (p40-GFP-Td cells) with ΔCD19-tagged control T cells and measured cell-surface binding of the p40–GFP fusion protein using an anti-GFP antibody conjugated to a far-red fluorochrome, to discriminate true extracellular binding of the p40–GFP protein from the GFP signal within cells (Fig. 6h). Upon TCR stimulation, both flow cytometry (Fig. 6i) and confocal microscopy (Fig. 6j) showed abundant GFP binding on the cell surface of p40-GFP-Td cells, but not on ΔCD19-Td cells, even when p19 and p40–GFP heterodimers could readily be detected in the culture medium (Fig. 6g). These data confirm the preferential binding of IL-23 to the T cells producing it. One possible explanation for the preferential binding of IL-23 to IL-23-producing T cells is that IL-23 is captured by IL-23R on p40-Td cells before its diffusion. To test this hypothesis, we used soluble recombinant human IL-23R (rhIL-23R) that binds IL-23, preventing its engagement with the IL-23R expressed by T cells (Supplementary Fig. 15b).

**Fig. 5 | p40 expression enhances the antitumor activity of T cells in syngeneic tumor models. a**,**b**, Expression of *Il23a* and *Il12b* (**a**) and of *Il23r* (**b**) as determined by qRT–PCR in ex vivo-activated and expanded mouse splenic T cells after re-stimulation with anti-CD3/CD28 antibodies for 0, 24 and 48 h. Data are represented as the fold change in gene expression, normalized to the housekeeping gene *Cd3e* and to the value at time 0. Data are shown as individual values and the mean ± s.d. ($n=4$). **c**, Measurement of mouse IL-23 released by mouse splenic T cells transduced with either empty vector (EV) or vector encoding mouse *Il12b* (mp40-Td) and re-stimulated with anti-CD3/CD28 antibodies for 0, 24 and 48 h. Data are shown as individual values and the mean ± s.d. ($n=8$). $^{**}P=0.0055$, $^{****}P<0.0001$. **d**, Cell counts of EV and mp40-Td mouse T cells at days 1, 3 and 5 after re-stimulation with anti-CD3/CD28 antibodies. Data are shown as the mean ± s.d. ($n=3$). $^{****}P<0.0001$, determined by repeated-measures two-way ANOVA with Sidak's post hoc test. **e**, Schematic of the syngeneic B16-OVA melanoma model; s.c., subcutaneous. **f**, Measurement of tumor volume after tumor engraftment. Data are shown as the mean ± s.d. of two independent experiments. For experiments with $1\times10^6$ T cells, $n=5$ mice per group for wild-type (WT) cells and $n=8$ mice per group for OT-1-EV and OT-1-mp40-Td cells. For experiments with $2\times10^6$ T cells, $n=6$ mice per group for WT and OT-1-EV cells and $n=7$ mice per group for OT-1-mp40-Td cells. $^{*}P=0.0182$, $^{***}P=0.0007$, $^{****}P<0.0001$, determined by two-way ANOVA with Sidak's post hoc test. **g**, Detection of mouse IL-23 in serum and tumor supernatant collected 14 d after T cell infusion. Data are shown as individual values and the mean ($n=5$ mice per group for serum and $n=7$ mice per group for tumor supernatant). **h**, Frequency of OT-1 TCR$^+$ ($V_\alpha2^+V_\beta5^+$) cells among CD8$^+$ T cells in the tissues collected from treated mice. Data are shown as the mean ± s.d. ($n=5$ mice per group). $^{****}P<0.0001$, determined by two-way ANOVA with Sidak's post hoc test. **i**, Immune composition of peripheral blood, spleen, dLN and tumor at the time that mice were killed. Data are shown as individual values and the mean ± s.d. of two independent experiments ($n=9$ mice per group). **j**, Schematic of the syngeneic PDAC orthotopic model. Mouse cell line KPC-4662, engineered to express mouse B7-H3 (KPC-mB7-H3), was implanted ($0.1\times10^6$ cells per mouse) into the pancreas of 6-week-old C57BL/6 mice. Eighteen days after tumor cell implantation, mice were irradiated with 400 cGy and 3 d later were infused intravenously with syngeneic B7-H3.CAR.EV cells ($1\times10^7$ cells per mouse) or B7-H3.CAR.mp40-Td cells ($1\times10^7$ cells per mouse). Tumor growth was monitored by ultrasound. **k**, Summary of the mean fold change (compared to day 0) in tumor volume from two independent experiments ($n=8$ mice per group). $^{****}P<0.0001$, determined by two-way ANOVA with Sidak's post hoc test for comparison of B7-H3.CAR.EV cells with B7-H3.CAR.mp40-Td cells at day 42.

We found that, even when the IL-23 in diffusion was fully sequestered, the cell-surface binding of p40–GFP to p40-Td cells remained unchanged, as measured by both flow cytometry (Fig. 6k) and confocal microscopy (Fig. 6l). In addition, rhIL-23R did not hamper IL-23-mediated expansion of p40-Td cells (Fig. 6m), suggesting that free IL-23 does not contribute to the binding or function of IL-23 in p40-Td cells. Collectively, these data showed an autocrine mode of action of IL-23 that has limited effects on bystander cells.

## Discussion

In this study, we have demonstrated that providing the p40 subunit of IL-23 to tumor-specific T cells is sufficient to cause

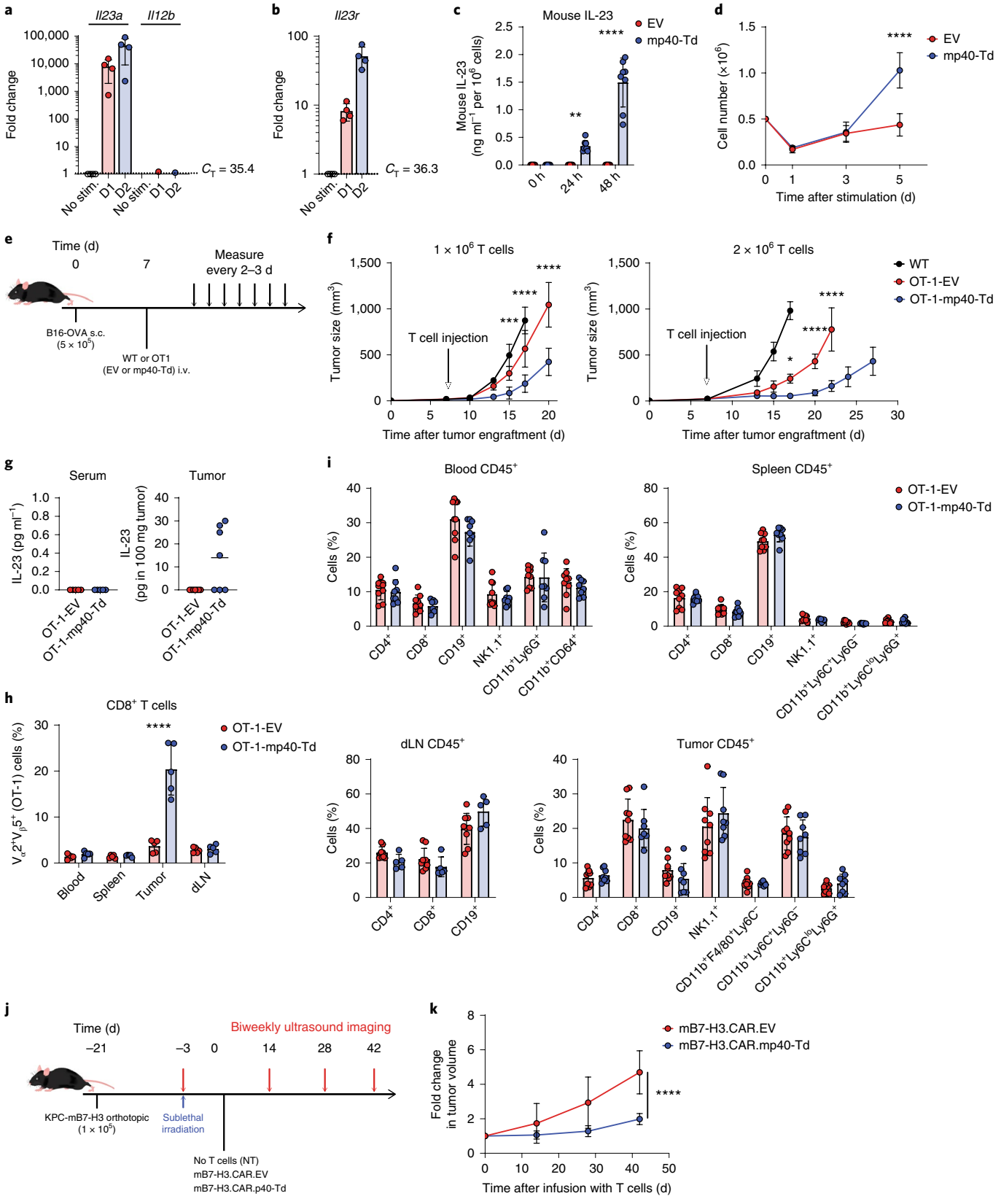

the production and release of IL-23. Furthermore, IL-23 exerts its function exclusively through activated T cells because both IL-23 production and IL-23R expression occur following T cell activation. This tightly regulated IL-23–IL-23R-engineered pathway is further controlled by an autocrine mode of action of the secreted IL-23 that prevents cytokine usage by other bystander immune cells.

The role of IL-23 in tumor cell growth remains controversial. Studies have shown that low amounts of endogenous IL-23 produced by tumor-associated macrophages, dendritic cells or tumor cells may promote inflammation, favoring early tumor initiation and progression[21,29,30,45]. IL-23 was also reported to promote metastasis in some CRC models[46]. On the contrary, high levels of IL-23, obtained either through IL-23 engineering of tumor cells or administration of recombinant IL-23, had antitumor effects[47,48]. Our data in multiple mouse models demonstrate the antitumor benefit of IL-23 when this cytokine is produced by engineered tumor-specific T cells, while no obvious side effects are exhibited, as compared to other previously reported cytokine engineering strategies. Furthermore, we observed that IL-23 by itself is not sufficient to promote the differentiation of ex vivo-generated tumor-specific T cells into IL-17-producing cells, the main culprit for promotion of carcinogenesis in IL-23-sensitive tumors such as CRC[30].

We have made the unexpected observation that the *IL23A* (p19) gene, but not the *IL12B* (p40) gene, is expressed in ex vivo-generated tumor-specific T cells when these cells are activated via engagement of either the endogenous TCR or an inserted CAR. Furthermore, the observed activation-dependent p19 expression is conserved in both mouse and human T cells and is especially pronounced in mouse T cells, where p19 expression is upregulated by more than 10,000-fold upon activation. Notably, p19 is sufficiently expressed to allow functional production and release of IL-23 if the p40 subunit is provided. To our knowledge, no specific functions have been attributed to the single p19 subunit. It is generally accepted that IL-23 in its heterodimeric form is assembled intracellularly and that p19 is not secreted as an independent protein nor in association with proteins other than p40 (refs. [18,49]). However, one study showed that human gastric carcinoma cells can secrete p19 in the absence of p40 subunit[50], which implies that the subunit may have IL-23-independent functions. Although our data suggest that *IL23A* knockdown does not have detrimental effects in T cells, a more exhaustive assessment of the function of p19 in T cells is warranted.

The p40 engineering we propose has multiple potential advantages. While a milieu of cytokines supporting T cell survival and proliferation is critical to obtaining antitumor effects after adoptive T cell therapies, the clinical experience demonstrates that toxic effects secondary to systemic and uncontrolled cytokine spread occur. The proposed p40 engineering restricts cytokine spread because IL-23 is released exclusively upon T cell activation within the TME. In fact, even if the p40 subunit is constitutively expressed in engineered T cells, IL-23 is only assembled when the p19 subunit is upregulated in response to T cell activation. Upon secretion within the TME, γ-chain cytokines can be used by a variety of immune cells that express the γ-chain receptor, which either amplifies or attenuates T cell-mediated immune responses[51,52]. In contrast, IL-23R expression is much more restricted and T cells releasing IL-23 express high levels of IL-23R. A similar scenario was previously modeled in the context of IL-2 and $T_{reg}$ cells, showing preferential capture of the cytokine by the cells producing it, thereby limiting diffusion and bystander effects[53,54]. Indeed, IL-23 released by p40-enginiered T cells is preferentially bound to the IL-23R expressed by the same cells. This model for IL-23 was supported by our data showing that sequestering of soluble IL-23 by soluble IL-23R did not reduce IL-23 binding and activity in p40-Td cells. Therefore, this autocrine mode of action of IL-23 further supports the improved specificity and safety of p40 engineering in tumor-specific T cells.

The generation of autologous cellular T cell products in patients with cancer has the caveat that T cells may be functionally impaired owing to age, specific disease or previous therapies the patient may have received. It was recently shown in patients with chronic lymphocytic leukemia, which is characterized by the presence of dysfunctional T cells, that activation of the STAT3 signaling pathway correlated with better performance of CAR T cells generated ex vivo[16,17]. Our data support the beneficial role of STAT3-associated pathways, which are induced by IL-23 through p40 engineering. Downstream of STAT3 signaling, we also observed enrichment of hypoxia-related genes in p40-Td cells. We speculate that this effect is possibly due to cooperative transactivation by STAT3 and HIF transcription factors[55,56]. Furthermore, this molecular profile resembles our previously described hypoxia signature in effector memory T cells, likely contributing to the proliferative and antiapoptotic functions of p40 (ref. [24]).

In summary, we describe a new strategy to incorporate a highly regulated cytokine signaling pathway into tumor-specific T cells that improves their efficacy. Our approach has substantial translational potential considering that it can be used for both CAR- and TCR-engineered T cells, as both TCR and CAR activation

**Fig. 6 | Engineered IL-23 functions predominantly through an autocrine mode of action. a**, Schematics of the co-activation experiment with p40-Td and ΔCD19-Td cells. **b**, Representative western blot showing the expression of IL-23R in ΔCD19-Td and p40-Td cells at days 1 and 3 after activation ($n=3$). **c**, Representative plots of NGFR$^+$ (p40-Td) cells and CD19$^+$ (bystander) cells at days 0 and 5 after activation. Data are representative of five independent experiments. **d**, Cell number and percentage of NGFR$^+$ and CD19$^+$ cells 5 d after activation. Data are shown as individual values and the mean ± s.d. ($n=5$). Dotted lines indicate starting cell number or percentage. ****$P<0.0001$, ***$P=0.0008$, determined by two-sided paired Student's *t*-test. **e**, Schematic of the sequential co-culture of GD2-specific CAR T cells coexpressing either ΔCD19 (CAR.ΔCD19-Td) or p40 (CAR.p40-Td) with the LAN-1 tumor cell line. **f**, Percentages of NGFR$^+$ and CD19$^+$ CAR T cells detected at the end of the first and second rounds of co-culture. Data are shown as individual values and the mean ± s.d. ($n=6$). ****$P<0.0001$, determined by repeated-measures two-way ANOVA with Sidak's post hoc test. **g**, Flow plot illustrating the coexpression of NGFR and GFP (left) and detection of IL-23 in the supernatant (right) for T cells transduced with a vector encoding the p40–GFP fusion protein. Data are shown as individual values and the mean ± s.d. ($n=4$). **h**, Schematics and staining procedure for the co-activation experiment with cells expressing p40–GFP and ΔCD19-Td cells. **i**, Representative flow histograms showing binding of p40–GFP protein on the cell surface of CD19$^+$ and NGFR$^+$ T cells. Data are shown as individual values and the mean ± s.d. ($n=5$). ***$P=0.0003$, determined by two-sided paired Student's *t*-test. **j**, Representative confocal microscopy imaging showing binding of p40–GFP protein on the cell surface of CD19$^+$ and NGFR$^+$ cells, representative of five independent experiments (left), and quantification of the fluorescence intensity of the cell-surface GFP signal for CD19$^+$ and NGFR$^+$ cells (right). Data are shown as individual values and the mean ± s.d. ($n=49$ cells for CD19$^+$ cells, $n=44$ cells for NGFR$^+$ cells). ****$P<0.0001$, determined by two-sided paired Student's *t*-test. **k**,**l**, Cell-surface binding of p40–GFP on p40-GFP-Td cells in the absence or presence of soluble rhIL-23R as determined by flow cytometry (**k**) and confocal microscopy (**l**). Data are shown as individual values and the mean ± s.d. ($n=5$ independent experiments for **k**, $n=25$ and 23 cells analyzed for the no treatment and rhIL-23R groups, respectively, in **l**). **m**, Number of Ctrl and p40-Td T cells 5 d after activation with anti-CD3/CD28 antibodies in the presence or absence of soluble rhIL-23R. Data are shown as individual values and the mean ± s.d. ($n=6$). ***$P=0.0006$, determined by repeated-measures two-way ANOVA with Sidak's post hoc test.

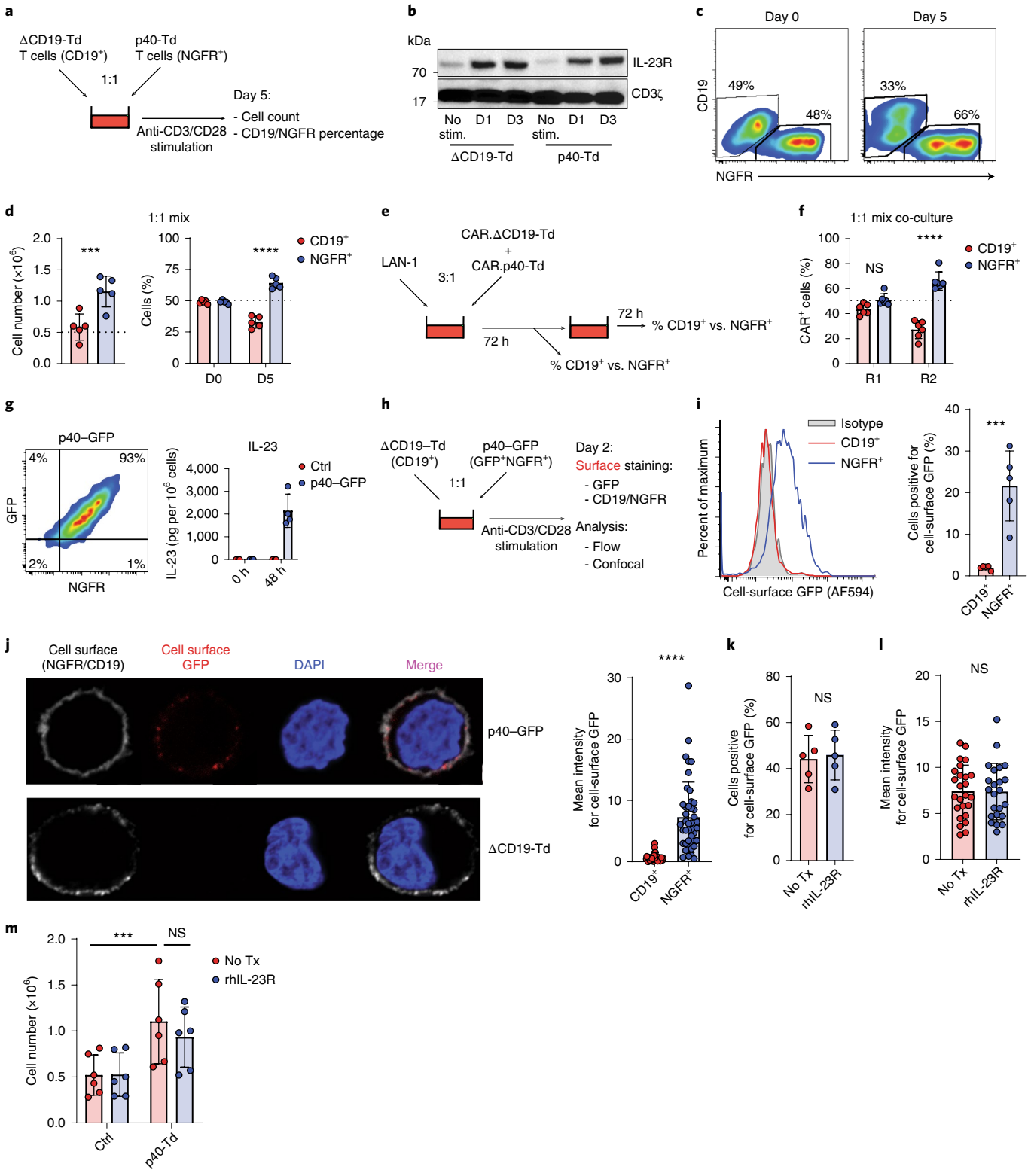


allow upregulation of IL-23R and the p19 subunit, and the endogenous p19 subunit can be coupled with the ectopically expressed p40 subunit.

## Online content

Any methods, additional references, Nature Research reporting summaries, source data, extended data, supplementary information, acknowledgements, peer review information; details of author contributions and competing interests; and statements of data and code availability are available at https://doi.org/10.1038/s41587-019-0398-2.

Received: 25 January 2019; Accepted: 17 December 2019;
Published online: 3 February 2020

## References

1. Garber, K. Driving T-cell immunotherapy to solid tumors. *Nat. Biotechnol.* **36**, 215–219 (2018).

2. D'Angelo, S. P. et al. Antitumor activity associated with prolonged persistence of adoptively transferred NY-ESO-1 $^{c259}$T cells in synovial sarcoma. *Cancer Discov.* **8**, 944–957 (2018).
3. Porter, D. L., Levine, B. L., Kalos, M., Bagg, A. & June, C. H. Chimeric antigen receptor-modified T cells in chronic lymphoid leukemia. *N. Engl. J. Med.* **365**, 725–733 (2011).
4. Maude, S. L., Teachey, D. T., Porter, D. L. & Grupp, S. A. CD19-targeted chimeric antigen receptor T-cell therapy for acute lymphoblastic leukemia. *Blood* **125**, 4017–4023 (2015).
5. Sanmamed, M. F. & Chen, L. A paradigm shift in cancer immunotherapy: from enhancement to normalization. *Cell* **175**, 313–326 (2018).
6. Anderson, K. G., Stromnes, I. M. & Greenberg, P. D. Obstacles posed by the tumor microenvironment to T cell activity: a case for synergistic therapies. *Cancer Cell* **31**, 311–325 (2017).
7. Kershaw, M. H., Westwood, J. A. & Darcy, P. K. Gene-engineered T cells for cancer therapy. *Nat. Rev. Cancer* **13**, 525–541 (2013).
8. Yao, X. et al. Levels of peripheral $CD4^{+}FoxP3^{+}$ regulatory T cells are negatively associated with clinical response to adoptive immunotherapy of human cancer. *Blood* **119**, 5688–5696 (2012).
9. Hurton, L. V. et al. Tethered IL-15 augments antitumor activity and promotes a stem-cell memory subset in tumor-specific T cells. *Proc. Natl Acad. Sci. USA* **113**, E7788–E7797 (2016).
10. Hoyos, V. et al. Engineering CD19-specific T lymphocytes with interleukin-15 and a suicide gene to enhance their anti-lymphoma/leukemia effects and safety. *Leukemia* **24**, 1160–1170 (2010).
11. Waldmann, T. A. et al. Safety (toxicity), pharmacokinetics, immunogenicity, and impact on elements of the normal immune system of recombinant human IL-15 in rhesus macaques. *Blood* **117**, 4787–4795 (2011).
12. Berger, C. et al. Safety and immunologic effects of IL-15 administration in nonhuman primates. *Blood* **114**, 2417–2426 (2009).
13. Di Stasi, A. et al. Inducible apoptosis as a safety switch for adoptive cell therapy. *N. Engl. J. Med.* **365**, 1673–1683 (2011).
14. Sockolosky, J. T. et al. Selective targeting of engineered T cells using orthogonal IL-2 cytokine–receptor complexes. *Science* **359**, 1037–1042 (2018).
15. Andersen, R. et al. Long-lasting complete responses in patients with metastatic melanoma after adoptive cell therapy with tumor-infiltrating lymphocytes and an attenuated IL2 regimen. *Clin. Cancer Res.* **22**, 3734–3745 (2016).
16. Kagoya, Y. et al. A novel chimeric antigen receptor containing a JAK–STAT signaling domain mediates superior antitumor effects. *Nat. Med.* **24**, 352–359 (2018).
17. Fraietta, J. A. et al. Determinants of response and resistance to CD19 chimeric antigen receptor (CAR) T cell therapy of chronic lymphocytic leukemia. *Nat. Med.* **24**, 563–571 (2018).
18. Oppmann, B. et al. Novel p19 protein engages IL-12p40 to form a cytokine, IL-23, with biological activities similar as well as distinct from IL-12. *Immunity* **13**, 715–725 (2000).
19. Duvallet, E., Semerano, L., Assier, E., Falgarone, G. & Boissier, M. C. Interleukin-23: a key cytokine in inflammatory diseases. *Ann. Med.* **43**, 503–511 (2011).
20. Ngiow, S. F., Teng, M. W. & Smyth, M. J. A balance of interleukin-12 and -23 in cancer. *Trends Immunol.* **34**, 548–555 (2013).
21. Iwakura, Y. & Ishigame, H. The IL-23/IL-17 axis in inflammation. *J. Clin. Invest.* **116**, 1218–1222 (2006).
22. Aggarwal, S., Ghilardi, N., Xie, M. H., de Sauvage, F. J. & Gurney, A. L. Interleukin-23 promotes a distinct CD4 T cell activation state characterized by the production of interleukin-17. *J. Biol. Chem.* **278**, 1910–1914 (2003).
23. Guedan, S. et al. ICOS-based chimeric antigen receptors program bipolar $T_H17/T_H1$ cells. *Blood* **124**, 1070–1080 (2014).
24. Xu, Y. et al. Glycolysis determines dichotomous regulation of T cell subsets in hypoxia. *J. Clin. Invest.* **126**, 2678–2688 (2016).
25. Langrish, C. L. et al. IL-23 drives a pathogenic T cell population that induces autoimmune inflammation. *J. Exp. Med.* **201**, 233–240 (2005).
26. Zhu, J., Yamane, H. & Paul, W. E. Differentiation of effector CD4 T cell populations. *Annu. Rev. Immunol.* **28**, 445–489 (2010).
27. Muranski, P. & Restifo, N. P. Essentials of Th17 cell commitment and plasticity. *Blood* **121**, 2402–2414 (2013).
28. Frankel, T. L. et al. Both CD4 and CD8 T cells mediate equally effective in vivo tumor treatment when engineered with a highly avid TCR targeting tyrosinase. *J. Immunol.* **184**, 5988–5998 (2010).
29. Langowski, J. L. et al. IL-23 promotes tumour incidence and growth. *Nature* **442**, 461–465 (2006).
30. Grivennikov, S. I. et al. Adenoma-linked barrier defects and microbial products drive IL-23/IL-17-mediated tumour growth. *Nature* **491**, 254–258 (2012).
31. Subramanian, A. et al. Gene set enrichment analysis: a knowledge-based approach for interpreting genome-wide expression profiles. *Proc. Natl Acad. Sci. USA* **102**, 15545–15550 (2005).
32. Gargett, T. et al. GD2-specific CAR T cells undergo potent activation and deletion following antigen encounter but can be protected from activation-induced cell death by PD-1 blockade. *Mol. Ther.* **24**, 1135–1149 (2016).
33. Philip, M. et al. Chromatin states define tumour-specific T cell dysfunction and reprogramming. *Nature* **545**, 452–456 (2017).
34. Wherry, E. J. T cell exhaustion. *Nat. Immunol.* **12**, 492–499 (2011).
35. Du, H. et al. Antitumor responses in the absence of toxicity in solid tumors by targeting B7-H3 via chimeric antigen receptor T cells. *Cancer Cell* **35**, 221–237 (2019).
36. Lee, J. W., Komar, C. A., Bengsch, F., Graham, K. & Beatty, G. L. Genetically engineered mouse models of pancreatic cancer: the KPC model (LSL-*Kras*$^{G12D/+}$; LSL-*Trp53*$^{R172H/+}$;*Pdx-1-Cre*), its variants, and their application in immuno-oncology drug discovery. *Curr. Protoc. Pharmacol.* **73**, 14.39.11–14.39.20 (2016).
37. Mirlekar, B., Michaud, D., Searcy, R., Greene, K. & Pylayeva-Gupta, Y. IL35 hinders endogenous antitumor T-cell immunity and responsiveness to immunotherapy in pancreatic cancer. *Cancer Immunol. Res.* **6**, 1014–1024 (2018).
38. Zeitouni, D., Pylayeva-Gupta, Y., Der, C. J. & Bryant, K. L. *KRAS* mutant pancreatic cancer: no lone path to an effective treatment. *Cancers* **8**, E45 (2016).
39. Hu, B. et al. Augmentation of antitumor immunity by human and mouse CAR T cells secreting IL-18. *Cell Rep.* **20**, 3025–3033 (2017).
40. Chmielewski, M. & Abken, H. CAR T cells releasing IL-18 convert to T-bet$^{high}$FoxO1$^{low}$ effectors that exhibit augmented activity against advanced solid tumors. *Cell Rep.* **21**, 3205–3219 (2017).
41. Avanzi, M. P. et al. Engineered tumor-targeted T cells mediate enhanced anti-tumor efficacy both directly and through activation of the endogenous immune system. *Cell Rep.* **23**, 2130–2141 (2018).
42. Chen, Y. et al. Eradication of neuroblastoma by T cells redirected with an optimized GD2-specific chimeric antigen receptor and interleukin-15. *Clin. Cancer Res.* **25**, 2915–2924 (2019).
43. Diaconu, I. et al. Inducible caspase-9 selectively modulates the toxicities of CD19-specific chimeric antigen receptor-modified T cells. *Mol. Ther.* **25**, 580–592 (2017).
44. Tey, S. K., Dotti, G., Rooney, C. M., Heslop, H. E. & Brenner, M. K. Inducible caspase 9 suicide gene to improve the safety of allodepleted T cells after haploidentical stem cell transplantation. *Biol. Blood Marrow Transplant.* **13**, 913–924 (2007).
45. Teng, M. W. et al. Opposing roles for IL-23 and IL-12 in maintaining occult cancer in an equilibrium state. *Cancer Res.* **72**, 3987–3996 (2012).
46. Zhang, L. et al. IL-23 selectively promotes the metastasis of colorectal carcinoma cells with impaired Socs3 expression via the STAT5 pathway. *Carcinogenesis* **35**, 1330–1340 (2014).
47. Lo, C. H. et al. Antitumor and antimetastatic activity of IL-23. *J. Immunol.* **171**, 600–607 (2003).
48. Overwijk, W. W. et al. Immunological and antitumor effects of IL-23 as a cancer vaccine adjuvant. *J. Immunol.* **176**, 5213–5222 (2006).
49. Floss, D. M., Schroder, J., Franke, M. & Scheller, J. Insights into IL-23 biology: from structure to function. *Cytokine Growth Factor Rev.* **26**, 569–578 (2015).
50. Hor, Y. T. et al. A role for RUNX3 in inflammation-induced expression of *IL23A* in gastric epithelial cells. *Cell Rep.* **8**, 50–58 (2014).
51. Pulliam, S. R., Uzhachenko, R. V., Adunyah, S. E. & Shanker, A. Common γ chain cytokines in combinatorial immune strategies against cancer. *Immunol. Lett.* **169**, 61–72 (2016).
52. Rochman, Y., Spolski, R. & Leonard, W. J. New insights into the regulation of T cells by $\gamma_c$ family cytokines. *Nat. Rev. Immunol.* **9**, 480–490 (2009).
53. Thurley, K., Gerecht, D., Friedmann, E. & Hofer, T. Three-dimensional gradients of cytokine signaling between T cells. *PLoS Comput. Biol.* **11**, e1004206 (2015).
54. Oyler-Yaniv, A. et al. A tunable diffusion–consumption mechanism of cytokine propagation enables plasticity in cell-to-cell communication in the immune system. *Immunity* **46**, 609–620 (2017).
55. Noman, M. Z. et al. The cooperative induction of hypoxia-inducible factor-1α and STAT3 during hypoxia induced an impairment of tumor susceptibility to CTL-mediated cell lysis. *J. Immunol.* **182**, 3510–3521 (2009).
56. Pawlus, M. R., Wang, L. & Hu, C. J. STAT3 and HIF1α cooperatively activate HIF1 target genes in MDA-MB-231 and RCC4 cells. *Oncogene* **33**, 1670–1679 (2014).

## Methods

**Cell lines.** The CHLA-255 neuroblastoma cell line was provided by L.S. Metelitsa of Baylor College of Medicine[57], and the LAN-1 cell line was obtained from M. Brenner at Baylor College of Medicine[58]. Human PDAC cell line BXPC-3 and T2 cells were purchased from the American Type Culture Collection (ATCC). Tumor cell lines were transduced to express eGFP and firefly luciferase (Ffluc) for co-culture and mouse experiments, respectively, as previously described[59]. Human tumor cell lines in this study (LAN-1, CHLA-255, BXPC-3, T2) were maintained in complete RPMI medium (500 ml RPMI-1640 (Gibco) supplemented with 10% FBS (Germini), 2 mM GlutaMAX (Gibco), 100 U ml$^{-1}$ penicillin and 100 µg ml$^{-1}$ streptomycin (Gibco)). Mouse melanoma B16-OVA cells were provided by B. Vincent at the University of North Carolina at Chapel Hill and were maintained in complete RPMI medium with addition of 100 µM β-mercaptoethanol (Fisher) and 500 µg ml$^{-1}$ G418 (Gibco) to maintain OVA expression. Mouse PDAC cell line KPC-mB7-H3 was established and described previously[35] and was maintained in complete RPMI medium. All cell lines were routinely tested for mycoplasma and for cell-surface expression of target antigens.

**Plasmid construction and retrovirus production.** Full-length human *IL12B* (accession NM_002187.3), human *IL18* (accession NM_001562.4), mouse *Il12b* (accession NM_001303244.1), mouse *Il18* (accession NM_008360.2) and mouse *Il15* (accession NM_008357.2) were amplified by PCR from cDNA clones purchased from Origene and cloned into the retroviral vector SFG. Human *IL12B* and *IL18* were then subcloned into SFG vector containing an internal ribosomal entry site (IRES) and a truncated NGFR selectable marker (p40(i)NGFR; Supplementary Fig. 1a). As control, we used an empty vector containing the IRES and the NGFR gene (Ctrl(i)NGFR). Mouse *Il12b*, *Il18* and *Il15* were subcloned into SFG vector containing an IRES and a GFP marker, using empty vector with IRES and GFP as the control. The shRNA construct for *IL23A* was purchased from Origene (HuSH-29TM), and the promoter and shRNA sequences were amplified by PCR and cloned into SFG vector with a reverse (3′-to-5′) orientation. The p40–GFP fusion protein was generated by fusing the coding region of *IL12B* (amino acids 1–328) to the GFP gene by fusion PCR and was cloned into the SFG(i)NGFR vector. The CAR constructs used in this study were described previously[42,60,61].

Retroviral supernatants used for transduction were prepared as previously described[62]. To transduce human T cells, retrovirus with RD114 envelope was used. For mouse T cell transduction, retrovirus was generated using packaging vector encoding Eco envelope protein.

**Transduction and expansion of human T cells.** Buffy coats from healthy donors were purchased from the Gulf Coast Regional Blood Center (Houston). Peripheral blood mononuclear cells (PBMCs) isolated with Lymphoprep density separation (Fresenius Kabi Norge) were activated on plates coated with 1 µg ml$^{-1}$ anti-CD3 (Miltenyi Biotec) and 1 µg ml$^{-1}$ anti-CD28 (BD Biosciences) agonistic monoclonal antibodies. On day 2, T lymphocytes were transduced with retroviral supernatants using retronectin-coated plates (Takara Bio). To generate CAR.Ctrl, CAR.p40-Td and CAR.IL18-Td cells, double transduction was performed sequentially (day 2, CAR transduction; day 3, Ctrl(i)NGFR, p40(i)NGFR or IL18(i)NGFR transduction). On day 4, transduced T cells were collected from retronectin-coated plates and expanded in complete T cell medium (45% RPMI-1640 and 45% Click's medium (Irvine Scientific) supplemented with 10% FBS (Hyclone), 2 mM GlutaMAX, 100 U ml$^{-1}$ penicillin and 100 µg ml$^{-1}$ streptomycin) with IL-7 (10 ng ml$^{-1}$; PeproTech) and IL-15 (5 ng ml$^{-1}$; PeproTech), changing the medium every 2–3 d (ref. [63]). On days 10–14 after transduction, cells were collected for in vitro and in vivo experiments. T cells were cultured in IL-7- and IL-15-depleted medium for 1 d before being used for in vitro assays.

**Preparation of ex vivo-expanded mouse T cells.** Mouse T cells were isolated using the Mojosort T cell isolation kit (BioLegend) from splenocytes obtained from C57BL/6J or C57BL/6-Tg(TcraTcrb)1100Mjb/J (OT-1) mice acquired from the Jackson Laboratory or in-house breeding. T cells were then stimulated on plates coated with 1 µg ml$^{-1}$ anti-mouse CD3 (eBioscience) and 1 µg ml$^{-1}$ anti-mouse CD28 (eBioscience) monoclonal antibodies for 48 h. Activated mouse T lymphocytes were transduced with retroviral supernatant using retronectin-coated plates with the same protocol used to transduce human T cells. After removal from the retronectin-coated plates, T cells were expanded in complete medium (RPMI-1640 (Gibco) supplemented with 10% FBS (Hyclone), 2 mM GlutaMAX, 100 µM β-mercaptoethanol, 100 U ml$^{-1}$ penicillin and 100 µg ml$^{-1}$ streptomycin) with IL-7 (10 ng ml$^{-1}$) and IL-15 (5 ng ml$^{-1}$), changing the medium every 2 d. On day 5, T cells were collected and used for subsequent assays.

**Quantitative real-time PCR.** RNA was extracted from cells with the RNeasy Plus kit (Qiagen), quantified by NanoDrop or Qubit and reverse transcribed into cDNA using Superscript VILO (Thermo). Quantitative real-time PCR was performed using the QuantStudio 6 Flex real-time PCR system (Thermo). The TaqMan system was used in most assays except for the validation of RNA-seq analysis (STAT3-regulated and hypoxia pathway genes), which used the SYBR Green system. For comparison of gene expression in human T cells, 18S RNA was used as a control for normalization. For assays in mouse T cells, *Cd3e* was used as a control gene for normalization. For assays in patient specimens, absolute quantification of copies was conducted using standard curves generated with plasmid containing *IL23A* or *IL12B* cDNA.

TaqMan primers for the following genes were purchased from Applied Biosystems: human *IL23A* (assay ID Hs00372324_m1), human *IL12B* (assay ID Hs01011518_m1), human 18S RNA (assay ID Hs03003631_g1), human *IL23R* (assay ID Hs00332759_m1), human *TBX21* (assay ID Hs00894392_m1), human *RORC* (assay ID Hs01076112_m1), human *IFNG* (assay ID Hs00989291_m1), mouse *Il23a* (assay ID Mm00518984_m1), mouse *Il12b* (assay ID Mm01288989_m1), mouse *Cd3e* (assay ID Mm01179194_m1) and mouse *Il23r* (assay ID Mm00519943_m1).

SYBR Green primers for the following genes were purchased from Sigma: 18S: forward, 5′-AACCCGTTGAACCCCATT-3′; reverse, 5′-CCATCCAATCGG TAGTAGCG-3′; *SOX2*: forward, 5′-ATAATAACAATCATCGGCGG-3′; reverse, 5′-AAAAAGAGAGAGGCAAACTG-3′; *SOCS3*: forward, 5′-CCTATTACATCTA CTCCGGG-3′; reverse, 5′-ACTTTCTCATAGGAGTCCAG-3′; *CEBPD*: forward, 5′-CAGACTTTTCAGACAAACCC-3′; reverse, 5′-TTTCGATTTCAAATGC TGC-3′; *ABCA1*: forward, 5′-GTGTTTCTGGATGAACCC-3′; reverse, 5′-TTCC ATTGACCATGATTGC-3′; *IFIT1*: forward, 5′-CTGCCTAATTTACAGCAACC-3′; reverse, 5′-TGATCCAAGACTCTGTTTTC-3′; *IFIT3*: forward, 5′-ATGAGTGA GGTCACCAAG-3′; reverse, 5′-CCTTGAAGTTCCAGGTG-3′; *USP18*: forward, 5′-TGGTTTACACAACATTGGAC-3′; reverse, 5′-ATCCTCTTCAATATCCTGG TG-3′; *CDKN2B*: forward, 5′-GACTAGTGGAGAAGGTGC-3′; reverse, 5′-TCA TCATGACCTGGATCG-3′; *HIF1A*: forward, 5′-AAAATCTCATCCAAGAA GCC-3′; reverse, 5′-AATGTTCCAATTCCTACTGC-3′; *EPAS1*: forward, 5′-CAG AATCACAGAACTGATTGG-3′; reverse, 5′-TGACTCTTGGTCATGTTCTC-3′; *BNIP3L*: forward, 5′-AGGCATCTATATTGGAAAGC-3′; reverse, 5′-GCTTAC AATGGTCTCAAGTT-3′; *PDK1*: forward, 5′-ATGATGTCATTCCCACAATG-3′; reverse, 5′-AAGAGTGCTGATTGAGTAAC-3′; *DDIT3*: forward, 5′-CTTTTCCA GACTGATCCAAC-3′; reverse, 5′-GATTCTTCCTCTTCATTTCCAG-3′; *DDIT4*: forward, 5′-AATGTAAGAGTAGGAAGGGG-3′; reverse, 5′-ACAGTTCTAGAT GGAAGACC-3′; *EGLN1*: forward, 5′-CCCAAATTTGATAGACTGCTG-3′; reverse, 5′-ACACCTTTTTCACCTGTTAG-3′; *EGLN3*: forward, 5′-ATCATTCA TAGCAGATGTGG-3′; reverse, 5′-ATATCTGGTTGCGTAAGAGG-3′.

**Immunoblot analysis.** Protein was extracted from cells using RIPA buffer (Thermo) supplemented with proteinase and phosphatase inhibitors (Thermo). The same amount of protein for each sample was separated on precast 4–15% gradient gels (Bio-Rad) by SDS–PAGE and transferred to PVDF membranes (Bio-Rad). The membranes were blocked with 5% milk in TBS with 5% Tween-20 and probed with primary antibodies at 4 °C overnight. Then, membranes were washed and incubated with secondary antibodies conjugated to HRP. The following primary and secondary antibodies were used: anti-IL-23R (Novus Biological; 1:1,000 dilution), anti-GAPDH (clone 6C5, Santa Cruz; 1:1,000 dilution), anti-phospho-STAT3 (Tyr705) (clone D3A7, Cell Signaling Technology; 1:1,000 dilution), anti-phospho-STAT3 (Ser727) (clone 6E4, Cell Signaling Technology; 1:1,000 dilution), anti-STAT3 (clone D3Z2G, Cell Signaling Technology; 1:1,000 dilution), anti-CD3ζ (clone 6B10.2, Santa Cruz; 1:1,000 dilution), goat anti-rabbit IgG-HRP (Santa Cruz; 1:3,000 dilution) and rabbit anti-mouse IgG-HRP (Santa Cruz; 1:3,000 dilution). Blot images were acquired with the ChemiDoc MP system (Bio-Rad), and densitometry was performed with Image Lab software (Bio-Rad).

**Flow cytometry.** For cell-surface staining, cells were incubated with antibodies at room temperature for 15 min or at 4 °C for 30 min. For intracellular staining, cells were fixed and permeabilized with Cytofix/CytoPerm (BD Biosciences) for 15 min at room temperature and washed with 1× PermWash (BD Biosciences). Subsequent staining was performed with 1× PermWash as the staining and wash buffer. For CellTrace Violet (CTV) staining, cells were labeled with 5 µM CTV (Thermo) before culture. In most assays, cells were stained with Zombie Aqua Live/Dead Discrimination dye (BioLegend) to exclude dead cells from analysis.

The following antibodies used for the flow cytometry analysis were obtained from BD Biosciences: APC-conjugated anti-CD4 (clone RPA-T4), FITC-conjugated anti-CD8 (clone RPA-T8), Alexa Fluor 700-conjugated anti-CD8 (clone RPA-T8), PE-conjugated anti-IL-17A (clone SCPL1362), Alexa Fluor 647-conjugated anti-IFN-γ (clone B27), Alexa Fluor 647-conjugated anti-CD271 (NGFR; clone C40-1457), APC-conjugated anti-CD45RO (clone UCHL1), PE-conjugated anti-CD45RA (clone H100), PE-Cy7-conjugated anti-CD28 (clone CD28.2), BV421-conjugated anti-CD27 (clone M-T271), PE-Cy7-conjugated anti-CD279 (PD-1; clone EH12.1), BV711-conjugated anti-Tim3 (clone 7D3), PE-conjugated anti-CD223 (LAG3; clone T47-530), Alexa Fluor 647-conjugated anti-Ki67 (clone B56), PE-conjugated Annexin V, 7AAD, PE-conjugated rat anti-mouse IgG1 (clone X56), APC-Cy7-conjugated anti-CD3 (clone SK7), PE-conjugated anti-granzyme B (clone GB11), PE-conjugated anti-CD101 (clone V7.1), PE-conjugated anti-TNF-α (clone MAB11), PE-conjugated anti-CD45 (clone HI30). FITC-conjugated rat anti-mouse CD19 (clone 1D3), APC-Cy7-conjugated hamster anti-mouse CD3e (clone 145-2C11), PE-conjugated rat anti-mouse Ly6G (clone 1A8), BV421-conjugated rat anti-mouse Ly6C (clone AL21), APC-Cy7-conjugated rat anti-mouse CD11b (clone M1/70), PerCP-Cy5.5-conjugated hamster anti-mouse CD11c (clone HL3),

PerCP-Cy5.5-conjugated rat anti-mouse CD4 (RM4-5), PE-conjugated rat anti-mouse $V_{\alpha}2$ TCR (clone B20.1) and FITC-conjugated rat anti-mouse $V_{\beta}5.1$ 5.2 TCR (clone MR9-4).

The following antibodies were obtained from Thermo: Alexa Fluor 647-conjugated anti-CD19 (clone SJ25-C1) and Alexa Fluor 594-conjugated anti-GFP (polyclonal).

The following antibodies were obtained from BioLegend: BV711-conjugated rat anti-mouse CD45 (clone 30-F11), APC-conjugated rat anti-mouse CD8 (clone 53-6.7), APC-conjugated rat anti-mouse CD64 (clone X54-5/7.1) and PE-Cy7-conjugated rat anti-mouse F4/80 (clone BM8).

Flow cytometry data were collected on a BD LSRFortessa (BD Biosciences) using BD FACSDIVA software, and the flow data were analyzed with FlowJo software (v9.32, Tree Star).

**Acquisition and processing of frozen patient tumor samples.** Frozen patient tumor specimens and matching adjacent normal tissues were obtained from the Tissue Procurement Facility at the University of North Carolina at Chapel Hill. For RNA extraction, 20–30 mg of frozen tissues was lysed using RLT buffer from the RNeasy Plus kit (Qiagen). To extract extracellular protein in interstitial fluid for IL-23 ELISA, 40 mg of frozen tissue was incubated in DPBS to obtain a single-cell suspension and the supernatant was collected. Total protein amount was quantified by Bradford assay (Bio-Rad), and 100 µg of protein was used for ELISA.

**RNA sequencing and GSEA.** Total RNA was extracted as described above, and the library was prepared by the High-Throughput Sequencing Facility (HTSF) at the University of North Carolina at Chapel Hill using the KAPA Stranded mRNA-Seq kit (Kapa Biosystems). Twelve samples were pooled and sequenced using a HiSeq 4000 (Illumina) with the high-output paired-end 50-bp setting ($>20\times10^6$ reads per sample). Sequencing reads were aligned to the human genome (hg38) with the STAR aligner (v2.4.2)[64] and subsequently quantified with Salmon (v0.8.2)[65]. Differential expression analysis was conducted with DESeq2 (v3.8)[66] running on R (v3.5.0). Genes with $\log_2$ (fold change) > 1 and an FDR less than 0.05 in comparisons of Ctrl and p40-Td cells were considered to be significant.

For the PCA plot, genes with low expression (<20 counts across six samples (three for Ctrl cells and three for p40-Td cells)) were filtered out and data were transformed with regularized-logarithm transformation.

GSEA was performed with GSEA v2 software (Broad Institute)[31] on genes that were differentially expressed between day 5 activated Ctrl and p40-Td cells. Gene sets specified in this study were as follows: DAUER_STAT3_TARGETS_UP (M12391): STAT3-upregulated genes[67], DAUER_STAT3_TARGETS_DN (M13696): STAT3-downregulated genes[67] and HALLMARK_HYPOXIA (M5891): genes upregulated in response to hypoxia.

Selected differentially expressed genes in the STAT3 or hypoxia pathways identified in RNA-seq were independently validated by qRT–PCR.

**In vitro repetitive co-culture assays.** Tumor cells ($2.5\times10^6$; LAN-1, CHLA-255 and BXPC-3, all labeled with GFP) were seeded in treated 12-well tissue culture plates for 24 h, after which $5\times10^4$ (effector to tumor (E:T)= 1:5) or $1.25\times10^5$ (E:T = 1:2) CAR T cells were added to the tumor cells. After 3–5 d (accounting for donor variability in cytotoxicity), tumor cells had been completely eradicated (round 1). All cells in the well were collected and washed with PBS, resuspended in fresh medium and added to a new plate seeded with $2.5\times10^6$ tumor cells for 3 d (round 2). This procedure was repeated one more time, if applicable (round 3). At the end of each round, a duplicate well was collected for counting of residual tumor cells ($GFP^+$) and CAR T cells ($CD3^+$) and other phenotypic analysis (granzyme B, PD-1, CD101) of CAR T cells by flow cytometry.

For cytokine production assays after repetitive co-culture, $3\times10^6$ tumor cells (LAN-1) were irradiated with 40 Gy before seeding to reduce tumor burden for T cells, after which $1\times10^5$ (E:T = 1:3) CAR T cells were co-cultured with tumor cells in the assay.

**Mouse experiments.** Male and female 6- to 8-week-old NSG (NOD/SCID/IL-$2R^{null}$) mice were purchased from the Animal Core Facility at the University of North Carolina at Chapel Hill. Male and female 6- to 8-week-old C57BL/6J and OT-1 mice were purchased from the Jackson Laboratory. All mice were housed in the Animal Core Facility at the University of North Carolina at Chapel Hill. All mouse experiments were performed in accordance with UNC Animal Husbandry and Institutional Animal Care and Use Committee (IACUC) guidelines and were approved by the UNC IACUC.

**Xenogeneic mouse models.** For metastatic neuroblastoma models, CHLA-Ffluc ($2\times10^6$) tumor cells were injected intravenously into 8- to 10-week-old female NSG mice. Two weeks later, mice were infused intravenously with GD2-specific CAR.Ctrl or CAR.p40-Td cells. Tumor progression was monitored weekly by bioluminescence imaging using the IVIS Lumina II in vivo imaging system (PerkinElmer). For re-challenge experiments, another dose of CHLA-Ffluc ($3\times10^6$) cells was injected intravenously at 4 weeks after T cell infusion. Mice were killed when signs of discomfort were detected by the investigators or as recommended by the veterinarian who monitored the mice three times a week. Peripheral blood, spleen and liver (the primary tumor site) were collected at the indicated time points to measure the expansion and persistence of infused T cells ($hCD45^+hCD3^+$) by flow cytometry.

For the orthotopic PDAC model, BXPC-3-Ffluc ($1\times10^5$) tumor cells were suspended in 25 µl of DPBS, mixed with 25 µl of Matrigel (Corning) and surgically implanted into the pancreas of 8- to 10-week-old male NSG mice as previously described[35]. Fourteen days after tumor cell inoculation, control-vector-transduced T cells (Ctrl cells), B7-H3-specific CAR.Ctrl cells or CAR.p40-Td cells were injected intravenously via tail injection ($2\times10^6$ cells per mouse). Tumor growth was monitored weekly by bioluminescence imaging using the IVIS Lumina II in vivo imaging system (PerkinElmer). In this model, engraftment does not induce lethality in mice even when they are left untreated for more than 8 weeks after T cell infusion. Mice were arbitrarily considered dead in survival analysis when the luciferase signal was at least 15-fold higher than the initial signal at week 0. All mice were killed at 8 weeks after T cell infusion, and peripheral blood, spleen and pancreas were collected to measure the persistence of infused T cells ($hCD45^+hCD3^+$) by flow cytometry.

**Syngeneic mouse models.** B16-OVA cells ($5\times10^5$ cells per mouse) were suspended in 50 µl of DPBS mixed with 50 µl of Matrigel (Corning) and were subcutaneously injected into the left flank of 7- to 8-week-old male C57BL/6 mice. Seven days after tumor engraftment, WT or OT-1-TCR T cells were infused intravenously. Tumor size was monitored every 2–3 d after T cell infusion with a caliper. Tumor volume was calculated as length × width × width × 0.5, as previously described[14], and mice with a volume >1,000 $cm^3$ were killed and blood, spleen, tumor and tumor dLN were collected for immunophenotyping by flow cytometry.

For the orthotopic PDAC model, the mouse tumor cell line KPC-4662 was engineered to express mB7-H3 and implanted into the pancreas of 6-week-old female C57BL/6J mice by surgery ($1\times10^5$ cells per mouse). Eighteen days after tumor cell implantation, mice were irradiated with 400 cGy to create a lymphodepleted environment. Two days after irradiation, mice were infused intravenously with syngeneic T cells ($1\times10^7$ cells per mouse). Tumor growth was monitored by ultrasound imaging biweekly. Some mice from the untreated group were killed at day 40 after tumor engraftment for immunohistochemistry staining of the TME.

**Confocal microscopy.** Cells were collected and divided equally into two groups. One group was stained with Alexa Fluor 594-conjugated mouse anti-GFP antibody (Thermo) and Alexa Fluor 647-conjugated anti-NGFR (BD Biosciences), while the other group was stained with Alexa Fluor 594-conjugated mouse anti-GFP antibody and Alexa Fluor 647-conjugated anti-CD19 antibody (Thermo). Cells were stained for 30 min at 4 °C and subsequently washed with ice-cold DPBS. Cells were then fixed with Cytofix (BD Biosciences) for 10 min at room temperature, washed with DPBS and loaded onto a glass slide using a Cytospin Cytocentrifuge (Thermo). Prolong Diamond Antifade Mountant with DAPI (Thermo) was applied before sealing the slide with a category 1.5 coverslip (Thermo). The slides were imaged using a Zeiss LSM710 microscope, and image data were analyzed with Fiji (ImageJ).

To quantify binding of p40–GFP fusion protein on the cell surface, the cell membrane was first defined on the basis of Alexa Fluor 647 signal (corresponding to anti-NGFR and anti-CD19 antibodies marking p40-Td and ΔCD19-Td cells, respectively). In parallel, an irrelevant area (either an area with no cells or intracellular space) was selected as a background area. The MFI of Alexa Fluor 594 signal (anti-GFP) was measured in the membrane and background areas, and the cell-surface binding of p40–GFP was calculated as MFI(membrane) – MFI(background).

**Statistical analysis.** Student's *t*-tests were used to determine statistically significant differences between two samples. When multiple-comparison analyses were required, statistical significance was evaluated by ANOVA (one or two way), followed by Sidak's post hoc analysis. If the data reflected measurement of one sample over time or under different conditions, repeated-measures ANOVA was used, followed by Sidak's post hoc analysis. All statistical analyses were performed with two-tailed tests. Graph generation and statistical analyses were performed using GraphPad Prism, version 7 (GraphPad Software). A $P$ value of less than 0.05 was considered statistically significant.

**Reporting Summary.** Further information on research design is available in the Nature Research Reporting Summary linked to this article.

## Data availability

The RNA-seq datasets generated and analyzed during the current study are not publicly available (the genetic information from primary human T cells in this study was not consented to be published in the public domain) and will be available from the corresponding authors upon request.

## References

57. Song, L. et al. Oncogene MYCN regulates localization of NKT cells to the site of disease in neuroblastoma. *J. Clin. Invest.* **117**, 2702–2712 (2007).

58. Tarek, N. et al. Unlicensed NK cells target neuroblastoma following anti-GD2 antibody treatment. *J. Clin. Invest.* **122**, 3260–3270 (2012).
59. Caruana, I. et al. Heparanase promotes tumor infiltration and antitumor activity of CAR-redirected T lymphocytes. *Nat. Med.* **21**, 524–529 (2015).
60. Louis, C. U. et al. Antitumor activity and long-term fate of chimeric antigen receptor-positive T cells in patients with neuroblastoma. *Blood* **118**, 6050–6056 (2011).
61. Du, H. et al. Antitumor responses in the absence of toxicity in solid tumors by targeting B7-H3 via chimeric antigen receptor T cells. *Cancer Cell* **35**, 221–237 (2018).
62. Vera, J. et al. T lymphocytes redirected against the κ light chain of human immunoglobulin efficiently kill mature B lymphocyte-derived malignant cells. *Blood* **108**, 3890–3897 (2006).
63. Xu, Y. et al. Closely related T-memory stem cells correlate with in vivo expansion of CAR.CD19-T cells and are preserved by IL-7 and IL-15. *Blood* **123**, 3750–3759 (2014).
64. Dobin, A. et al. STAR: ultrafast universal RNA-seq aligner. *Bioinformatics* **29**, 15–21 (2013).
65. Patro, R., Duggal, G., Love, M. I., Irizarry, R. A. & Kingsford, C. Salmon provides fast and bias-aware quantification of transcript expression. *Nat. Methods* **14**, 417–419 (2017).
66. Love, M. I., Huber, W. & Anders, S. Moderated estimation of fold change and dispersion for RNA-seq data with DESeq2. *Genome Biol.* **15**, 550 (2014).
67. Dauer, D. J. et al. Stat3 regulates genes common to both wound healing and cancer. *Oncogene* **24**, 3397–3408 (2005).

## Acknowledgements

This work was supported in part by the University Cancer Research Fund at the University of North Carolina at Chapel Hill (G.D.), R01-CA193140-03 from the National Cancer Institute (G.D.), 1R37-CA230786-01A1-01A1 from the National Institutes of Health (Y.P.-G.), W81XWH-19-1-0597 from the Department of Defense (Y.P.-G.) and W81XWH-18-1-0441 from the Department of Defense (H.D.). The UNC Small Animal Imaging Facility at the Biomedical Imaging Research Center, the Microscopy Services Laboratory and the Flow Cytometry Core Facilities are supported in part by an NCI Cancer Center Core Support Grant to the UNC Lineberger Comprehensive Cancer Center (P30-CA016086-40). The frozen tissues for RNA and protein extraction were obtained from the Tissue Procurement Facility at the UNC Lineberger Comprehensive Cancer Center. We thank C. Santos and the Animal Studies Core Facility for providing mice and surgery services for the orthotopic pancreatic cancer mouse models.

## Author contributions

X.M., G.D. and Y.X. designed the experiments, analyzed data and wrote the manuscript. X.M. and Y.X. performed the experiments. P.S., Y.C., H.D., C.S., N.P.K., D.M., S.A., B.S., Y.P.-G. and S.Z. provided critical help and discussion for experiments. C.S., B.V. and Y.X. performed analysis on RNA-seq data.

## Competing interests

G.D. and B.S. have sponsored research agreements with Bluebird Bio, Cell Medica and Bellicum Pharmaceutical. G.D. serves on the scientific advisory board of MolMed and Bellicum Pharmaceutical.

## Additional information

**Supplementary information** is available for this paper at https://doi.org/10.1038/s41587-019-0398-2.

**Correspondence and requests for materials** should be addressed to G.D. or Y.X.

**Reprints and permissions information** is available at www.nature.com/reprints.